nature communications

Article

https://doi.org/10.1038/s41467-025-60750-0

HDL-bound S1P affects the subventricular niche and early neuropathological features of Alzheimer's disease

Received: 21 May 2024

Accepted: 28 May 2025

Published online: 01 July 2025

Check for updates

Byung Jo Choi[1,2], Ju Yeon Hong[1,2], Min Hee Park[1,2], Kang Ho Park[1,2], Wan Hui Han[1,2], Hee Ji Yoon[1,2], Hye Yoon Jung[1,2], Kyung Yeol Kim[1,2], Sun Ae Lee[1,2], Eun Young Lim[1,2], Jung Woo Hur[1,2], Im-Sook Song[3], So Yeon Jeon[4], Min-Koo Choi[4], Christina Christoffersen[5,6], Hee-Jin Kim[7], Seung Hyun Kim[7], Edward H. Schuchman[8], Jae-sung Bae[1,2] ✉ & Hee Kyung Jin[1,9] ✉

Circulating blood factors are critical for homeostasis of the adult ventricular-subventricular (V-SVZ) and subgranular zones, which contain neural stem cells (NSCs) crucial for sustained neurogenesis. Circulating sphingosine-1-phosphate (S1P) bound to apolipoprotein M (ApoM), a principal component of high-density lipoproteins, is involved in various biological processes, but its role in neurogenic niches is poorly understood. Herein, using *Apom*$^{-/-}$ mice, we show that blood ApoM-S1P deficiency impairs the SVZ-NSC pool, neurogenesis, ependymal cell polarity, and cerebrospinal fluid flow, leading to olfactory dysfunction and ventricular enlargement, early neuropathological features of Alzheimer's disease (AD). Enhancing the complex significantly rescues these defects by activating S1P1 receptor signaling in SVZ-NSCs. Consistently, blood ApoM-S1P levels are reduced in early AD patients and correlate with olfactory deficits and ventricular enlargement. Similar abnormalities are recapitulated in young APP/PS1 mice and reversed by restoring blood ApoM-S1P levels. Thus, these data reveal pathogenic mechanisms underlying early neuropathological features of AD and identify the blood ApoM-S1P complex as a potential diagnostic and therapeutic target.

Sphingosine-1-phosphate (S1P), an important regulatory sphingolipid, is enriched in circulatory fluids. S1P binds to G protein-coupled S1P receptors (S1PRs) to regulate embryonic development, postnatal organ function, and several pathological pathways related to type 2 diabetes and Alzheimer's disease (AD)[1–3]. The majority (~65 %) of plasma S1P is complexed with apolipoprotein M (ApoM), whereas the remainder is found in the lipoprotein-free fraction, presumably associated with albumin[4]. Circulating ApoM is predominantly associated with a specific population of high-density lipoprotein (HDL) particles and acts as the natural transporter for plasma S1P[5]. This blood ApoM-

[1]KNU AD Research Institute, Kyungpook National University, Daegu, South Korea. [2]Department of Physiology, Cell and Matrix Research Institute, School of Medicine, Kyungpook National University, Daegu, South Korea. [3]BK21 FOUR Community-Based Intelligent Novel Drug Discovery Education Unit, Vessel-Organ Interaction Research Center (VOICE), College of Pharmacy and Research Institute of Pharmaceutical Sciences, Kyungpook National University, Daegu, South Korea. [4]College of Pharmacy, Dankook University, Cheon-an, South Korea. [5]Department of Clinical Biochemistry, Rigshospitalet, Blegdamsvej 9, Copenhagen, Denmark. [6]Department of Biomedical Sciences, University of Copenhagen, Blegdamsvej 3A, Copenhagen, Denmark. [7]Department of Neurology, College of Medicine, Hanyang University, Seoul, South Korea. [8]Department of Genetics and Genomic Sciences, Icahn School of Medicine at Mount Sinai, New York, New York, USA. [9]Department of Laboratory Animal Medicine, College of Veterinary Medicine, Kyungpook National University, Daegu, South Korea. ✉e-mail: jsbae@knu.ac.kr; hkjin@knu.ac.kr

S1P complex regulates important physiological actions such as immunological functions, vascular development, vascular tone control, cardiac function, and vascular permeability[6–8].

The adult ventricular-subventricular zone (V-SVZ), located in the walls of the brain ventricles, consists of the SVZ and ventricular zones (VZ). The SVZ maintains pool of neural progenitor cells[9,10], and these cells continuously replace old interneurons in the olfactory bulb (OB), establishing a continuous cell turnover essential for the correct functioning of the OB, and, consequently, for olfaction[11,12]. The VZ is composed of multi-ciliated ependymal cells forming a robust barrier between the brain parenchyma and the ventricle lumen[13]. In this area, ependymal cells extend their motile cilia into the brain ventricles, contributing to cerebrospinal fluid (CSF) flow[14].

The adult V-SVZ niche primarily contains an extensive planar vascular plexus, notably devoid of astrocyte end feet and pericyte coverage[15]. This specialized property of the V-SVZ facilitates the passive passage of blood-borne factors, influencing the homeostasis of the V-SVZ niche[16]. Specifically, neural stem cells (NSCs) in the adult V-SVZ niche communicate with the vascular system by receiving blood-derived signals that regulate their proliferation and function[17–19]. In conditions such as AD and Parkinson's disease (PD), the two most prevalent neurodegenerative conditions in the elderly, there are fewer proliferating cells in the SVZ and ependymal cell dysfunction has been observed in the VZ as well[20–22]. Notably, olfactory impairment and ventricular enlargement are common and early signs of AD and PD[23–25], but the reasons for these are largely unknown. Therefore, we investigated the neuropathophysiological role of the blood ApoM-S1P complex in the regulation of the V-SVZ niche and its association with early symptoms of AD and PD.

Here, we show that the blood ApoM-S1P complex preserves V-SVZ homeostasis by maintaining neural progenitor cells, ependymal polarity, and CSF flow, thereby preventing olfactory dysfunction and ventricular enlargement, which are early neuropathological features of AD.

Results

The blood ApoM-S1P complex is required for maintenance of the NSC pool in the SVZ

To investigate the influence of the blood ApoM-S1P complex on neurogenic niches in vivo, ApoM-deficient (*Apom*$^{-/-}$) mice were used[26]. The levels of S1P were significantly reduced in both plasma and HDL of these mice compared to those in wild-type (WT) mice (Fig. 1a). Moreover, to determine whether the blood ApoM-S1P complex influences S1P levels in the brain, we measured the concentration of S1P in the extracellular extract from the SVZ, hippocampus, cortex, and olfactory bulb. The results showed a significant decrease in S1P concentration in the SVZ extracellular extract of *Apom*$^{-/-}$ mice compared to WT mice, but no reduction in the extracellular extracts from other brain regions (Fig. 1a and Supplementary Fig. 1a–c). These results indicate that the reduction of the ApoM-S1P complex in the blood specifically contributes to a decrease of S1P concentration in the SVZ extracellular extract, and it may be due to the unique vascular structure of the SVZ, which facilitates the delivery of blood-derived factors[16]. To directly confirm the transport of the ApoM-S1P complex from the blood to the SVZ, hippocampus, cortex, and olfactory bulb, we performed additional experiments using a stable isotope-labeled ApoM-S1P complex. This approach allowed us to trace the movement of the complex across the blood-brain barrier (BBB). Mass spectrometry detected the isotope-labeled S1P in the SVZ, providing direct evidence that the ApoM-S1P complex successfully crosses the BBB and accumulates in this region (Supplementary Fig. 1d). Additionally, the calculated brain-to-plasma partition coefficient (Kp) was 0.659, indicating efficient transport of the complex into the brain. In contrast, the hippocampus, cortex, and olfactory bulb exhibited significantly lower Kp values of 0.008, 0.014 and 0.008, respectively, suggesting minimal transport of the complex to these regions. These findings align with the observed S1P concentrations in extracellular extracts from the SVZ, hippocampus, cortex, and olfactory bulb, further supporting the role of the blood ApoM-S1P complex in selectively regulating S1P levels in the SVZ (Fig. 1a and Supplementary Fig. 1a–c). Furthermore, we investigated whether the blood ApoM-S1P complex could also reach the choroid plexus (CP), a region characterized by fenestrated capillaries, similar to the SVZ. The results showed that the blood ApoM-S1P complex efficiently reached the CP, with a Kp of 0.501. Given the critical role of the CP in CSF production, we examined whether ApoM-S1P is present in the CSF. Our analysis confirmed that ApoM is present in the CSF of WT mice but undetectable in *Apom*$^{-/-}$ mice, whereas its levels are elevated in *Apom*^{TG} mice (Supplementary Fig. 1e). Additionally, CSF S1P levels were significantly reduced in *Apom*$^{-/-}$ mice compared to WT controls and increased in *Apom*^{TG} mice (Supplementary Fig. 1f). These findings provide direct evidence that the ApoM-S1P complex from the blood preferentially accumulates in regions with fenestrated capillaries, such as the SVZ and CP, and plays a role in maintaining extracellular S1P levels, including in the CSF.

We next analyzed the NSC pool in the SVZ and subgranular zone (SGZ) of the hippocampus of these mice, revealing a significant decline in the population of SOX2^{+}GFAP^{+} NSCs in the SVZ of *Apom*$^{-/-}$ mice compared to WT mice (Fig. 1b). This reduction subsequently led to a decrease in MASH1^{+} neural progenitors and DCX^{+} newly generated neurons and neural precursor cells within the same region (Fig. 1c, d). However, in the dentate gyrus (DG) of the SGZ, the number of SOX2^{+}GFAP^{+} NSCs, DCX^{+} newly formed neurons, and NeuN^{+}BrdU^{+} mature differentiated neurons remained unchanged, which is consistent with the data that S1P concentration in the hippocampal extracellular extracts did not alter in *Apom*$^{-/-}$ mice (Supplementary Figs. 1a and 2). Therefore, these data suggested that deficiency of the blood ApoM-S1P complex results in NSC pool impairment, particularly in the SVZ neurogenic niche. Next, we confirmed whether the reduction of the SVZ-NSC pool is related to NSC proliferation or apoptosis. To analyze activated NSCs and their proliferation in vivo, BrdU was administered to 3-month-old WT and *Apom*$^{-/-}$ mice 3 weeks before sacrifice. In the SVZ, BrdU is selectively retained in some activated NSCs and newborn neurons that have stopped dividing in the OB[27]. We observed a notable decrease in SOX2^{+}GFAP^{+}BrdU^{+} cells in the SVZ of *Apom*$^{-/-}$ mice, along with a diminished proportion of these cells expressing the proliferation marker Ki67 (Fig. 1e). Consistent with these findings, the yield of primary neurospheres, originating from microdissected SVZ, similarly diminished in these mice (Fig. 1f). These results showed that the blood ApoM-S1P complex regulated the number of activated NSCs and their proliferation in the SVZ. In contrast, there was no significant difference in apoptosis using immunohistochemistry to assess cleaved caspase-3, the terminal deoxynucleotidyl transferase-mediated deoxyuridine triphosphate nick end labeling (TUNEL) assay, and by determining the expression levels of pro- or anti-apoptotic genes (Fig. 1g, h). Taken together, these findings suggested that the absence of the blood ApoM-S1P complex negatively impacts maintenance of the NSC pool and their proliferation in the SVZ, without altering apoptosis.

The blood ApoM-S1P complex is important for regulation of SVZ neurogenesis and olfactory function

The influence of the blood ApoM-S1P complex on maintenance of the SVZ-NSC pool pointed towards a potential effect on neurogenesis, leading us to quantify the number of adult newly formed neurons in the OB. Labeling proliferating cells with BrdU and analyzing the OB three weeks later revealed a significant decrease in BrdU^{+} newly formed neurons within the granule cell (GCL) and glomerular layers (GL) of *Apom*$^{-/-}$ mice (Fig. 2a). In adult mice, the majority of newly generated SVZ neurons migrating to the OB incorporate into the granule cell layer as NeuN-positive, GABAergic granule cells[28]. A smaller fraction becomes glutamatergic, GABAergic, or dopaminergic

https://doi.org/10.1038/s41467-025-60750-0

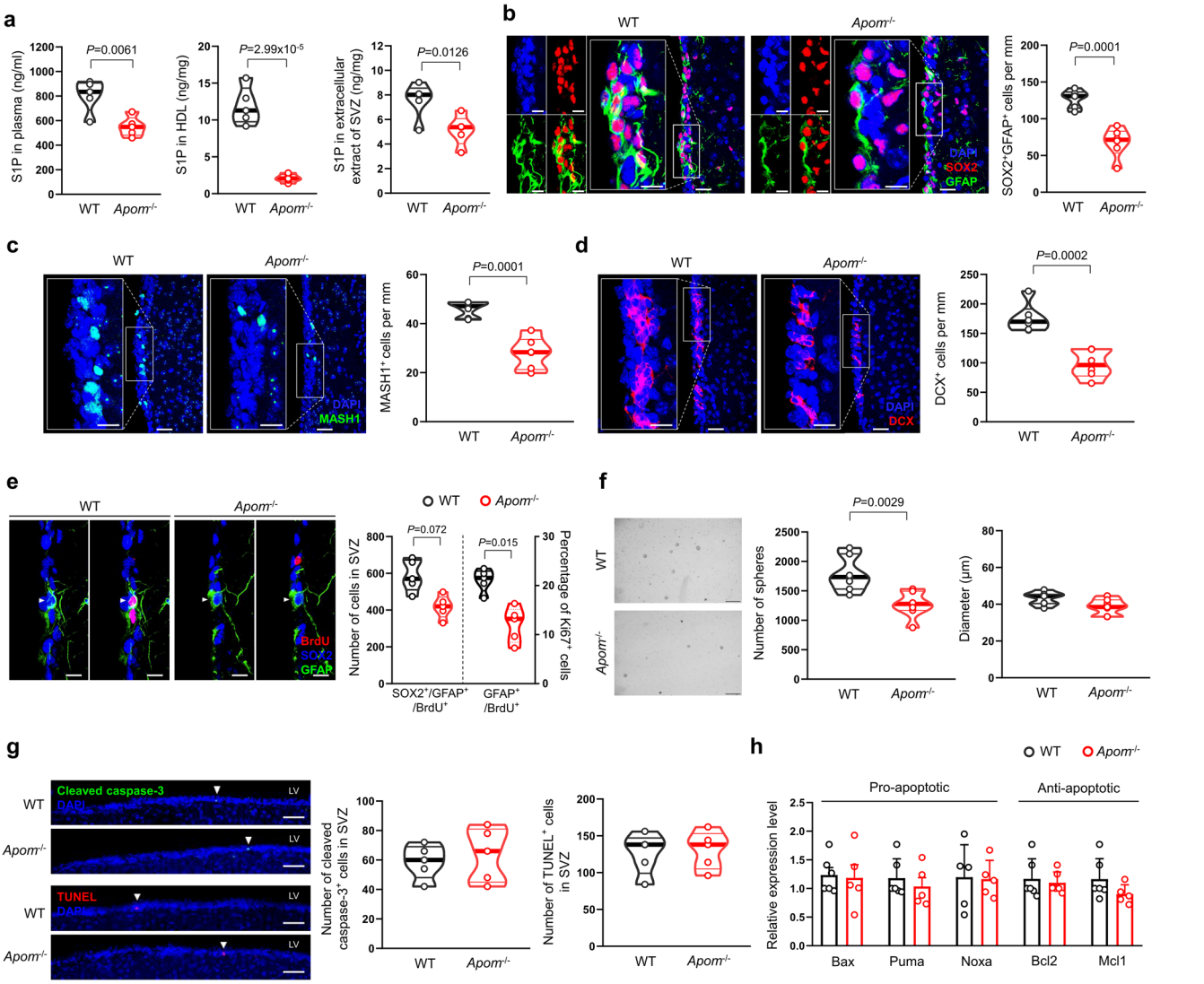

Fig. 1 | Depletion of blood ApoM-S1P complex causes abnormality of the NSC pool in the SVZ. a S1P concentration (n = 5/group). **b–d** Representative immunofluorescence images and quantification of SOX2$^+$GFAP$^+$ cells (**b**), MASH1$^+$ cells (**c**), and DCX$^+$ cells (**d**) in the SVZ (n = 6/group). Scale bars, 30 μm (enlarged, 15 μm) **e** Representative immunofluorescence images of SOX2$^+$GFAP$^+$BrdU$^+$ cells (left) and quantification of SOX2$^+$GFAP$^+$BrdU$^+$ cells and GFAP$^+$BrdU$^+$Ki67$^+$ cells (right) in the SVZ (n = 5/group). Scale bars, 10 μm. **f** Representative images (left), number (middle), and diameter (right) of primary neurospheres (n = 7/group). Scale bars, 300 μm. **g** Representative immunofluorescence images and quantification of cleaved caspase-3$^+$ and TUNEL$^+$ cells in the SVZ (n = 5/group). Scale bars, 50 μm. **h** mRNA levels of pro- and anti-apoptotic genes in the SVZ (WT, n = 6; *Apom*$^{-/-}$, n = 5). **a–f** Two-tailed student's t test. All error bars indicate s.e.m. All data analysis was done at 4-month-old mice. Source data are provided as a Source Data file.

periglomerular interneurons, classified into distinct populations based on the expression of calbindin (CB), calretinin (CR), or tyrosine hydroxylase (TH)[29,30]. These newborn interneurons contribute to the plasticity of the local circuitry by modulating the activity of mitral and tufted cells, playing a pivotal role in the processing of odor information[11,31]. Deficiency of the blood ApoM-S1P complex in *Apom*$^{-/-}$ mice induced a significant decrease in the density of CB$^+$, CR$^+$, and TH$^+$ interneurons in the glomerular layer (GL) of the OB (Fig. 2b), suggesting a potential olfactory dysfunction.

To explore whether these cellular changes observed in the OB of *Apom*$^{-/-}$ mice impact olfactory function, behavioral assays were performed. As predicted, we observed abnormalities of olfactory function in *Apom*$^{-/-}$ mice in the olfactory habituation/dishabituation test. These mice showed normal responses to a neutral scent (water) but lacked increased exploration for peanut butter and urine scents, unlike their WT littermates (Fig. 2c, d). Additionally, in olfactory avoidance tests, which assess innate aversion to specific odors, *Apom*$^{-/-}$ mice exhibited diminished avoidance responses to low amounts of non-dihydrogenated TMT (nTMT) (1 μl). Although, at higher amount (10 μl), the similar avoidance behaviors were observed between the two groups because the stimulus was so strong that it overrides the sensitivity impairment, these data indicated impaired sensitivity to these odors in *Apom*$^{-/-}$ mice (Fig. 2e). Next, to evaluate the olfactory discrimination capabilities, we conducted an olfactory discrimination test using two closely related odorants. In this test, food-restricted animals were trained to associate the odorant 2-methylbutyric acid (2MB) with sugar rewards. After a five-day training period, we placed two odorants, 2MB and cyclobutanecarboxylic acid (CB), separately beneath the bedding without any sugar rewards. We then compared the digging times for the two odorants within the same animal (Test 1). Although *Apom*$^{-/-}$ mice were able to distinguish between 2MB and CB, which are competing odorants, this olfactory discrimination ability was relatively poor compared to WT mice (Fig. 2f). To further confirm whether the mice were capable of detecting odorants buried under the cage bedding in test 1, additional tests were performed using only 2MB in test 2 and only CB in test 3, respectively. In test 2, *Apom*$^{-/-}$ mice spent

https://doi.org/10.1038/s41467-025-60750-0

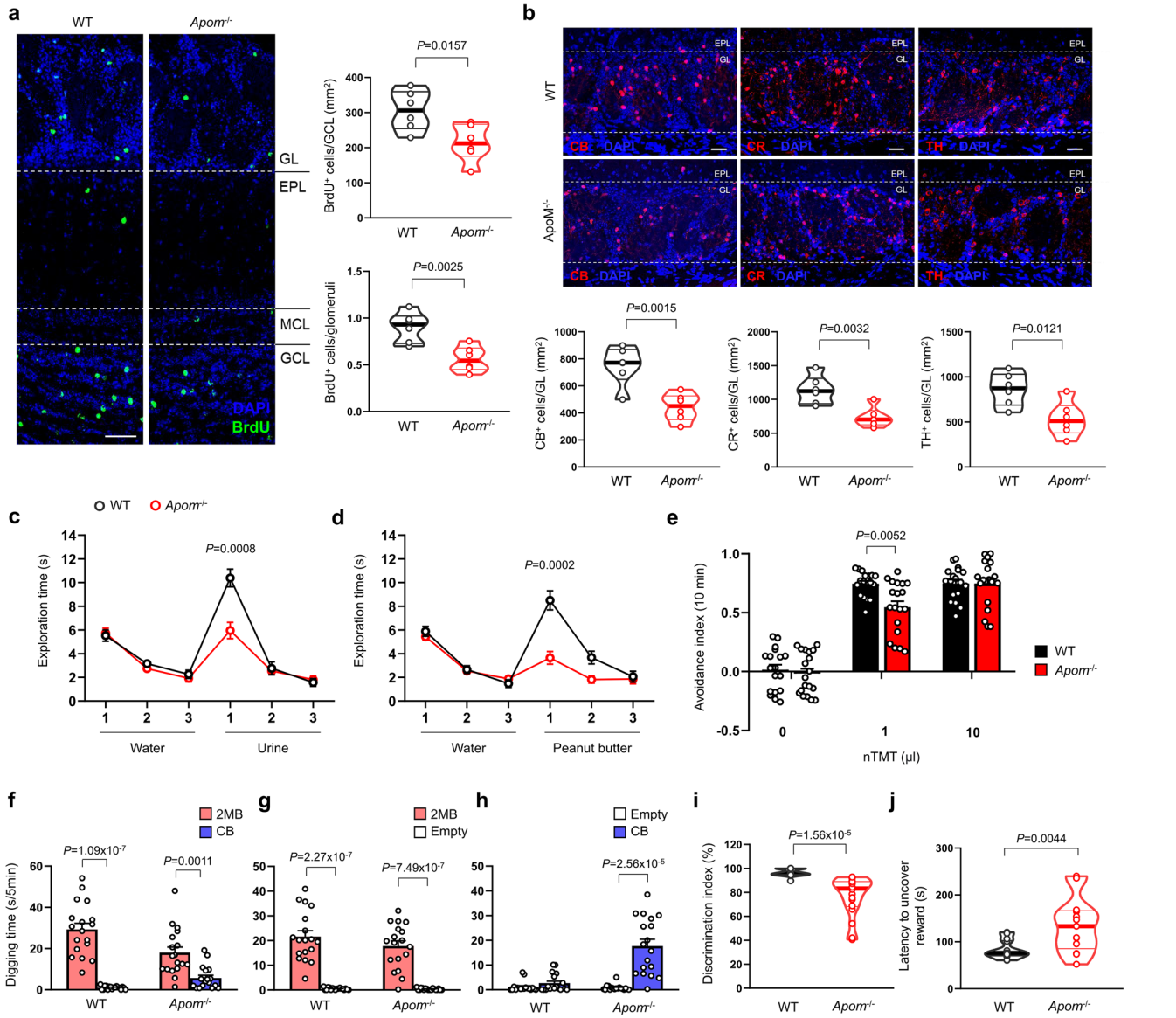

Fig. 2 | Depletion of blood ApoM-S1P complex impairs SVZ neurogenesis and olfaction. a Representative immunofluorescence images (left) and quantification of BrdU$^+$ newly formed neurons in the GCL (right upper) and GL (right lower) in the OB (n = 6/group). Scale bars, 30 µm. **b** Representative immunofluorescence images and quantification of CB$^+$ cells, CR$^+$ cells, TH$^+$ cells in GL (n = 6/group). Scale bars, 30 µm. **c, d** The results of olfactory habituation–dishabituation test for both urine (**c**) and peanut butter (**d**) scents (WT, n = 16; *Apom*$^{-/-}$, n = 19). **e** The results of olfactory avoidance test (WT, n = 18; *Apom*$^{-/-}$, n = 19). **f**–**i** The results of the olfactory discrimination test 1 (**f**), test 2 (**g**), test 3 (**h**), and calculated a discrimination index of the data points shown in f (i) (n = 18/group). **j** The latency to locate a buried food reward (WT, n = 14; *Apom*$^{-/-}$, n = 13). **a, b, i, j** Two-tailed student's t test. **c**–**h** Two-way ANOVA for repeated measures. All error bars indicate s.e.m. All data analysis was done at 4-month-old mice. Source data are provided as a Source Data file.

significantly more time digging near the 2MB previously associated with a sugar reward, similar to WT mice (Fig. 2g). However, intriguingly, during test 3, these mice also spent a considerable amount of time digging near the CB-scented area, despite it not being associated with a sugar reward, unlike the WT mice, which showed no preference for the CB-scented area (Fig. 2h). Moreover, the discrimination index, where '1' represents exclusive digging at the 2MB site and '0' indicates equal amounts of digging at both the 2MB and CB sites, was significantly lower in *Apom*$^{-/-}$ mice compared to WT mice (Fig. 2i). The ability of food-deprived mice to locate a buried food reward was also impaired in the *Apom*$^{-/-}$ mice (Fig. 2j), indicating impairment of olfactory discrimination ability. Of note, contrary to the olfactory dysfunction results, general activity, anxiety, and both spatial and associative memory remained unaffected in *Apom*$^{-/-}$ mice (Supplementary Fig. 3a-o). Collectively, these data demonstrated that the blood ApoM-S1P complex plays a critical role in maintaining olfactory function by regulating SVZ neurogenesis.

Deficiency of the blood ApoM-S1P complex causes loss of ependymal cell polarity, impaired CSF flow, and LV enlargement

In the adult lateral ventricle (LV), NSCs are repositioned from the VZ into the SVZ by ependymal cells[32]. This relocation establishes NSCs and ependymal cells as components of the SVZ neurogenic niche, which is marked by its distinctive cytoarchitecture and cell-cell interactions[32,33]. In this regard, we examined the impact of the blood ApoM-S1P complex on ependymal cell function in the VZ. To visualize the cilium on the ependymal cells, we performed immunofluorescence staining for acetylated α-tubulin, a marker of motile cilia. In WT mice, acetylated α-tubulin exhibited a uniform distribution on the ependymal cells lining the walls of the LV, indicating a consistent ciliary structure. In contrast,

https://doi.org/10.1038/s41467-025-60750-0

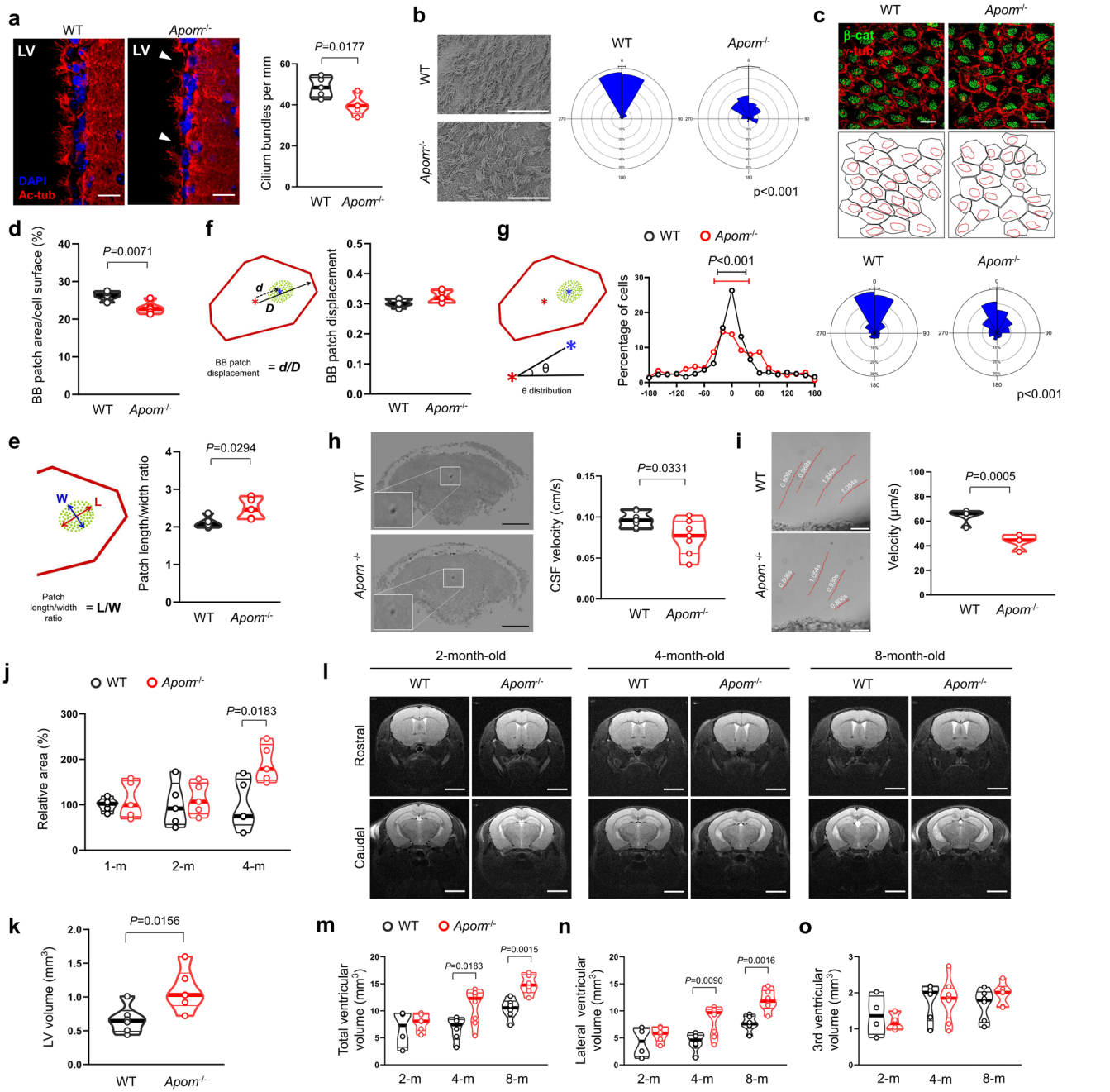

Fig. 3 | Depletion of blood ApoM-S1P complex induces loss of polarity in ependymal cells, leading to LV enlargement. a Representative immunofluorescence images and quantification of cilium bundles in LV ($n = 5$/group). Scale bars, 15 μm. **b** Representative scanning electron microscopy images and angular distribution of vectors representing the orientation of ciliary tufts (WT, $n = 104$; *Apom*$^{-/-}$, $n = 100$; five animals/group). Scale bars, 30 μm. **c** Representative confocal images of wholemount staining of β-catenin (β-cat; green) and γ-tubulin (γ-tub; red) in the walls of LVs (upper) and traces of the apical surfaces and BB patches (lower). Scale bars, 10 μm. **d** Quantification of BB patch area in the walls of LVs ($n = 5$/group). **e** Distribution of the percentage of cells with different length/width ratios of the BB patches (WT, $n = 442$; *Apom*$^{-/-}$, $n = 414$; five animals/group). **f** Quantification of BB patch displacement (WT, $n = 441$; *Apom*$^{-/-}$, $n = 413$). **g** Histogram of the distribution (left) and angular distribution (right) of BB patch angles in ependymal cells (WT, $n = 441$; *Apom*$^{-/-}$, $n = 413$; five animals/group). **h** Representative MRI images and quantification of CSF flow in the cerebral aqueduct ($n = 7$/group). Scale bars, 2 mm. **i** Representative images overlaid with microbead movement paths captured through motion tracking (lines) and quantification of velocity of microbeads propelled by cilia at the surface ($n = 5$/group). Scale bar: 30 μm. **j** Quantification of LV areas ($n = 5$/group). **k** Quantification of LV volume ($n = 6$/group). **l** Representative MRI images of the rostral and caudal brain. Scale bars, 3 mm. **m**–**o** Quantification of total ventricle volume (m), LV volume (n), and 3rd venticular volume (o) from the 2-month-old (WT, $n = 4$; *Apom*$^{-/-}$, $n = 6$), 4-month-old (WT, $n = 6$; *Apom*$^{-/-}$, $n = 8$), and 8-month-old (WT, $n = 6$; *Apom*$^{-/-}$, $n = 6$) mice. **a, d, f, h**–**k, m**–**o** Two-tailed student's *t* test. **b, g** Two-sided Watson U^2 test. **e** Contingency table test. All data analysis was done at 4-month-old mice, with the exception of l-o. Source data are provided as a Source Data file.

Apom$^{-/-}$ mice showed an abnormal and discontinuous staining pattern in ependymal cells for acetylated α-tubulin, and cilium bundles were also reduced in these mice (Fig. 3a). We then assessed the motile cilia on the surface of the LV using scanning electron microscopy (SEM). WT ependymal cells exhibited uniformly oriented cilium bundles, while *Apom*$^{-/-}$ ependymal cells showed disarray in cilia orientation (Fig. 3b). To further examine the association between ciliary abnormalities and changes in the planer cell polarity of ependymal cells due to

the deficiency of the blood ApoM-S1P complex, we analyzed the morphology and polarity of ciliary basal bodies using whole-mount staining of LV. The results showed that the ependymal cells of *Apom*$^{-/-}$ mice displayed irregular cilia patches in comparison to their WT counterparts (Fig. 3c). Moreover, there was a notable decrease in the percentage of the apical surface area covered by basal body (BB) patches in *Apom*$^{-/-}$ mice, pointing to a compromised ciliary density (Fig. 3d). The BB patches observed in *Apom*$^{-/-}$ mice exhibited a higher length-to-width ratio, indicating a more elongated shape relative to those found in WT mice (Fig. 3e). While the displacement of BB patches was unchanged, analysis of BB patch angles showed increased variability in these mice (Fig. 3f, g), implying that *Apom*$^{-/-}$ ependymal cells deviated from the uniform planar polarity observed in healthy ependymal cells. Therefore, these observations demonstrated that a deficiency of the blood ApoM-S1P complex led to a compromise in the structural integrity and planar polarity of ciliary basal body patches in ependymal cells, potentially affecting their function.

The dysfunction and disruption of ependymal cell polarity in the SVZ has been implicated in the impairment of CSF circulation[34,35], and it has been well demonstrated in stroke mouse model[36], suggesting a potential for CSF flow abnormalities in *Apom*$^{-/-}$ mice. Based on this, we analyzed CSF flow using magnetic resonance imaging (MRI) by measuring CSF movement through the cerebral aqueduct in live mice. Furthermore, ciliary motility was assessed by employing high-speed video microscopy to monitor microbead movement across the surface of brain ventricles ex vivo. The result showed a significant reduction in CSF flow in *Apom*$^{-/-}$ mice compared to their WT littermates (Fig. 3h). Ependymal cilia in *Apom*$^{-/-}$ mice propelled microbeads at a significantly slower rate than observed in WT mice (Fig. 3i). Interestingly, *Apom*$^{-/-}$ mice exhibited ventricular enlargement, likely due to abnormal CSF circulation in vivo. We observed an increase in both total and LV volumes in these mice compared with WT mice (Fig. 3j–n). However, the volume of the 3rd ventricle was unchanged across all time points in *Apom*$^{-/-}$ mice (Fig. 3o), indicating that the ventricular enlargement due to the blood ApoM-S1P complex deficiency was specific to the LV. Despite the LV enlargement observed in *Apom*$^{-/-}$ mice, the volumetric characteristics of the total brain, cortex, and hippocampus, as well as the brain and body weight, were comparable to those of their WT littermates (Supplementary Fig. 4a–e). We further evaluated the potential blockage within the ventricular system by administering Evans blue dye into the LV, because ventricular expansion is known to be associated with aqueductal stenosis[37]. Five minutes after injection, the dye was observed in both the contralateral and 4th ventricles, indicating a lack of obstruction in both *Apom*$^{-/-}$ mice and their WT littermates (Supplementary Fig. 4f). Consistent with these observations, we detected no structural changes in the aqueduct (Supplementary Fig. 4g). These results highlighted that the blood ApoM-S1P complex is required to maintain normal CSF circulation through the regulation of the structure and function of ependymal cell cilia within the ventricular system.

In addition, to investigate whether V-SVZ neurogenesis impaired by blood ApoM-S1P complex deficiency was entirely related to postnatal/adult neurogenesis, we examined the number of cells in the SVZ and OB of newborn *Apom*$^{-/-}$ mice (postnatal data 0, P0). The results showed that there were no significant changes in the number of NSCs (BLBP$^+$ cells) in the SVZ and interneurons (CB$^+$, CR$^+$, TH$^+$ cells) in the OB of P0 *Apom*$^{-/-}$ mice (Supplementary Fig. 5a, b). Moreover, H&E staining revealed no significant structural abnormalities or ventricular enlargement in the brains of these mice (Supplementary Fig. 5c), suggesting that the blood ApoM-S1P complex deficiency does not affect the development of the SVZ and OB in mice, and primarily contribute to impairment of postnatal/adult V-SVZ neurogenesis.

According to the data of Fig. 1a and Supplementary Fig. 1d, blood ApoM-S1P complex successfully crosses the BBB and contributed to S1P levels in the SVZ. Based on these results, to clarify the critical role of the blood ApoM-S1P complex in regulating the SVZ neurogenic niche, 2-month-old *Apom*$^{-/-}$ mice were intravenously injected with serum from *Apom*$^{-/-}$ or ApoM transgenic (*Apom*^{TG})[26] mice twice a week for 8 weeks. As expected, *Apom*$^{-/-}$ mice injected with *Apom*^{TG} mice serum showed an increase in the number of SOX2$^+$GFAP$^+$ NSCs, MASH1$^+$ neural progenitors, and DCX$^+$ newly generated neurons and neural precursor cells in the SVZ (Supplementary Fig. 6a–c). The number of SOX2$^+$GFAP$^+$BrdU$^+$ cells and their proliferation also increased in these mice (Supplementary Fig. 6d, e). Moreover, *Apom*^{TG} serum enhanced BrdU$^+$ newly formed neurons within the GCL and GL, as well as the density of CB$^+$, CR$^+$, and TH$^+$ interneurons in the GL of *Apom*$^{-/-}$ mice (Supplementary Fig. 6f, g), leading to improvement of olfactory dysfunction (Supplementary Fig. 6h–k).

To further examine the functional impact of the ApoM-S1P complex in HDL on SVZ-NSCs, SVZ-NSCs derived from WT mice were treated with either ApoM$^-$HDL or ApoM$^+$HDL. Interestingly, ApoM$^+$HDL induced a significant increase in SVZ neurosphere formation. The increase in neurosphere formation mediated by ApoM$^+$HDL was effectively blocked by pre-incubation with an anti-S1P antibody compared with control antibody treatment (Supplementary Fig. 6l), indicating that S1P associated with ApoM$^+$HDL is essential for the self-renewal capacity of SVZ-NSCs. Contrary to the neurosphere formation result, these was no difference in NSC proliferation or cell death, evidenced by the diameter of the neurospheres (Supplementary Fig. 6m). Therefore, these results suggested that S1P associated with ApoM$^+$HDL plays a vital role in the self-renewal processes of SVZ-NSCs, but not in proliferation. Similarly, when examining the effects of ApoM-S1P on SGZ-NSCs, ApoM$^+$HDL also enhanced neurosphere formation, and this effect was blocked by pre-incubation with an anti-S1P antibody (Supplementary Fig. 6n). However, as observed in SVZ-NSCs, neurosphere size remained unchanged, indicating no effect on NSC proliferation or survival (Supplementary Fig. 6o). Interestingly, these in vitro findings contrast with previous in vivo data, which showed that blood ApoM-S1P did not alter the NSC pool in the SGZ (Supplementary Fig. 2). This discrepancy suggests that differences in the transport and availability of blood ApoM-S1P within the NSC niche may underlie a brain-region-specific regulation of ApoM-S1P, distinguishing its effects in the SVZ from those in the SGZ (Fig. 1a and Supplementary Fig. 1a–d).

Next, the transplantation of *Apom*^{TG} serum into *Apom*$^{-/-}$ mice also corrected the disruption of basal body polarity in ependymal cells (Supplementary Fig. 7a–e). This treatment further enhanced CSF flow within the cerebral aqueduct and ciliary motility, resulting in mitigation of ventricular enlargement in *Apom*$^{-/-}$ mice (Supplementary Fig. 7f–h). To exclude the possibility that *Apom*^{TG} serum might induce changes in other blood factors due to ApoM overexpression, which could indirectly influence the V-SVZ neurogenic niche, we performed additional experiments using WT serum. Treatment with WT serum resulted in a slight increase in the SVZ-NSC pool and the number of newly formed neurons and interneurons in the OB of *Apom*$^{-/-}$ mice (Supplementary Fig. 8a–f). These results suggest that the blood ApoM-S1P complex exerts a direct regulatory effect on the V-SVZ neurogenic niche and olfactory function, rather than being mediated by other factors altered by ApoM overexpression. However, these improvements were less pronounced compared to those observed with *Apom*^{TG} serum treatment, likely due to the lower ApoM-S1P complex content in WT serum relative to *Apom*^{TG} serum, which was insufficient to fully restore the V-SVZ neurogenic niche. To further clarify the specific role of the blood ApoM-S1P complex, we intravenously administered isolated ApoM$^-$HDL or ApoM$^+$HDL complex to *Apom*$^{-/-}$ mice. Treatment with ApoM$^+$HDL significantly improved the V-SVZ neurogenic niche by enhancing the SVZ-NSC pool, restoring olfactory behavior, correcting basal body polarity in ependymal cells, improving CSF flow, and normalizing ciliary motility and LV size (Supplementary Fig. 9). Importantly, these effects were absent when ApoM$^-$HDL complex were administered, underscoring the indispensable role of the ApoM-S1P complex in mediating these processes. Taken

together, these findings demonstrated the critical effects of the circulating ApoM-S1P complex in promoting SVZ neurogenesis and preventing ependymal cell defects in *Apom*$^{-/-}$ mice, suggesting potential therapeutic value in treating neurological disorders associated with these abnormalities.

ApoM-S1P-S1PR1 signaling regulates the V-SVZ neurogenic niche through the ERK pathway

S1P associated with ApoM$^+$HDL interacts with five G protein-coupled receptors (S1PR1-S1PR5) and regulates a plethora of biological actions[8,38,39]. Quantitative RT-PCR (qPCR) assays showed that *S1pr1* was the most abundantly expressed among S1P receptors in the adult SVZ of WT mice, and its expression was the predominant in NSCs isolated from the SVZ (Supplementary Fig. 10a, b). Furthermore, digital PCR analysis revealed that absolute mRNA expression levels of *S1pr1* were significantly higher in NSCs compared to endothelial cells and astrocytes isolated from the SVZ, demonstrating that NSCs are the predominant expressors of *S1pr1* (Supplementary Fig. 10c). We then evaluated S1PR1 protein expression in the SVZ using S1PR1-enhanced green fluorescent protein (eGFP) (*Edg1*$^{eGFP/eGFP}$) mice in which the WT receptor was replaced with fluorescently tagged S1PR1[40]. These mice exhibited stronger expression of S1PR1 in the SVZ lining of the ventricles, especially in SOX2$^+$GFAP$^+$ NSCs than in SOX2$^-$GFAP$^+$ astrocytes, DCX$^+$ newly generated neurons and neural precursor cells, S100β$^+$ ependymal cells and CD31$^+$ endothelial cell (Supplementary Fig. 10d–f). Consistent with these observations, S1PR1 protein was also found in Nestin$^+$ neural progenitors isolated from the SVZ of WT mice (Supplementary Fig. 10g). Moreover, we confirmed S1PR1 activation in SVZ-NSCs in vivo using S1PR1-GFP signaling reporter mice, wherein receptor activation triggers a nuclear GFP signal[41]. In these mice, SOX2$^+$GFAP$^+$ NSCs exhibited active S1PR1 signaling within the SVZ, whereas S1PR1-independent H2B-GFP activity was minimally observed in the SVZ and absent in NSCs of H2B-GFP mice, indicating the functional engagement of this signaling pathway in NSCs (Supplementary Fig. 10h). The essential role of the blood ApoM-S1P complex in activating S1PR1 signaling within SVZ-NSCs is also supported by the reduced S1PR1 signaling observed in SVZ-NSCs of S1PR1-GFP signaling reporter mice lacking ApoM (S1PR1-GFP; *Apom*$^{-/-}$), in contrast to control littermates. Remarkably, the transplantation of *Apom*^{TG} serum into these mice reversed the decrease of S1PR1 signaling in SVZ-NSCs (Supplementary Fig. 10i). Therefore, these findings indicated that S1P associated with ApoM$^+$HDL directly interacts with S1PR1 on SVZ-NSCs, suggesting a potential role of blood ApoM-S1P-S1PR1 signaling in modulating the V-SVZ neurogenic niche.

To elucidate that the role of blood ApoM-S1P-S1PR1 signaling in the V-SVZ resides within the adult GFAP$^+$ neural stem cell population, a murine genetic model (*S1pr1*$^{\Delta GFAP}$) was created by breeding mice that have loxP sites flanking part of the *S1pr1* gene (*S1pr1*$^{loxp/loxp}$) with mice that express inducible Cre-recombinase under the GFAP promoter's control (*GFAP*-CreERT2). Subsequent analysis confirmed a marked reduction in both *S1pr1* mRNA and protein levels in SVZ-NSCs isolated from tamoxifen-treated *S1pr1*$^{\Delta GFAP}$ mice, in comparison to their untreated counterparts, referred to as control mice (Supplementary Fig. 11a). These mice showed a pronounced decrease in the SVZ-NSC pool, as observed in *Apom*$^{-/-}$ mice (Supplementary Fig. 11b–d). This reduction is further evidenced by diminished counts of SOX2$^+$GFAP$^+$BrdU$^+$ cells, lower Ki67 expression within these cells, and significantly decreased primary neurospheres (Supplementary Fig. 11e, f). Moreover, *S1pr1* deletion in the SVZ-NSCs led to a lower number of BrdU$^+$ newly formed neurons and interneurons in the OB, ultimately resulting in defects of olfactory behavior and perception (Supplementary Fig. 11g–k). Intriguingly, we also observed disrupted basal body polarity of ependymal cells, diminished CSF flow, compromised ciliary motility, and enlarged ventricles in *S1pr1*$^{\Delta GFAP}$ mice (Supplementary Fig. 11l–r), indicating that ApoM-S1P-S1PR1 signaling in the SVZ-NSCs preserved the structural and functional integrity of ependymal cells rather than survival of the ependymal cells themselves. Since GFAP Cre-recombinase is expressed not only in NSCs but also in astrocytes, we further confirmed the functional role of this signaling using *Split-GFAP/CD133*cre, which specifically drives Cre expression in GFAP$^+$CD133$^+$ NSCs[42,43]. Two-month-old *S1pr1*$^{fl/fl}$ mice were daily injected with *Split-GFAP/CD133*cre into the lateral ventricles for 2 months, and we observed the reduction in both *S1pr1* mRNA and protein levels in the SVZ-NSCs of *Split-GFAP/CD133*cre; *S1pr1*$^{fl/fl}$ mice (Supplementary Fig. 12a). These mice showed the decrease in the SVZ-NSC pool, defects of olfactory behavior, disrupted basal body polarity of ependymal cells, diminished CSF flow, compromised ciliary motility, and enlarged ventricles as observed in *S1pr1*$^{\Delta GFAP}$ mice (Supplementary Fig. 12b–r), demonstrating that ApoM-S1P-S1PR1 signaling in the SVZ-NSCs is mainly responsible for regulating V-SVZ neurogenic niche. To further validate our findings, we utilized an additional neural stem cell-specific Cre mouse model, *Nestin*-CreERT2, crossed with *S1pr1*$^{loxp/loxp}$ mice to generate *S1pr1*$^{\Delta Nestin}$ mice. Analysis of these mice demonstrated results consistent with those observed in *S1pr1*$^{\Delta GFAP}$ and *Split-GFAP/CD133*cre; *S1pr1*$^{fl/fl}$ mice, strongly reinforcing the conclusion that ApoM-S1P-S1PR1 signaling within SVZ-NSCs plays a critical role in regulating and maintaining the V-SVZ neurogenic niche (Fig. 4).

A previous study reported that impaired S1PR1 signaling in brain endothelial cells can lead to BBB defects[44], which raises the possibility that these disruptions may affect NSC renewal, differentiation, and/or migration within the V-SVZ neurogenic niche. Thus, to investigate this possibility, we generated *S1pr1*$^{\Delta Cdh5}$ mice by crossing *S1pr1*$^{fl/fl}$ mice and *Cdh5*-creERT2 mouse, which express Cre protein in endothelial cells[45,46]. The data showed that S1PR1 mRNA expression and protein levels were successfully suppressed in the isolated SVZ microvessels from *S1pr1*$^{\Delta Cdh5}$ mice. (Supplementary Fig. 13a). However, we found no significant changes in SVZ neurogenesis, olfactory function, and LV expansion in the brain of these mice (Supplementary Fig. 13b–r). These data indicated that ApoM-S1P-S1PR1 signaling in the brain vasculature did not influence on V-SVZ neurogenic niche, further supporting that this signaling in the SVZ-NSCs plays a major role in regulating the V-SVZ neurogenic niche.

To more verify the effects of blood ApoM-S1P-S1PR1 signaling in the NSCs on regulation of the V-SVZ neurogenic niche, *S1pr1*$^{\Delta Nestin}$ mice lacking ApoM (*S1pr1*$^{\Delta Nestin}$ mice; *Apom*$^{-/-}$) were injected with *Apom*$^{-/-}$ or *Apom*^{TG} serum. The results showed no significant improvement of the abnormal V-SVZ neurogenic niche between groups (Supplementary Fig. 14). Similar findings were observed in *S1pr1*$^{\Delta GFAP}$ mice lacking ApoM (*S1pr1*$^{\Delta GFAP}$; *Apom*$^{-/-}$) (Supplementary Fig. 15). Overall, these findings revealed that the blood ApoM-S1P complex contributed to the regulation of the V-SVZ neurogenic niche by enhancing postnatal neurogenesis and ensuring the structural and functional integrity of ependymal cells, through S1PR1 in the NSCs.

Next, to better understand the mechanism of ApoM-S1P-S1PR1 signaling in the NSCs on the regulation of the V-SVZ neurogenic niche, we conducted a neurosphere formation assay using SVZ-NSCs from control or *S1pr1*$^{\Delta GFAP}$ mice. Treatment with ApoM$^+$HDL significantly enhanced neurosphere formation of SVZ-NSCs from control mice while this process was disrupted in S1PR1-deficient cells (Fig. 5a), supporting the importance of ApoM-S1P-S1PR1 signaling in the self-renewal of SVZ-NSCs. Subsequently, RNA sequencing (RNA-seq) analysis was performed to comprehensively assess the gene expression changes in this setting. We identified 348 differentially expressed genes (DEGs) between ApoM$^-$HDL and ApoM$^+$HDL-treated control NSCs, setting a threshold of p-value ≤ 0.05 and requiring a fold change of more than two. Intriguingly, 324 DEGs were exclusively identified in the control SVZ-NSCs group, but not in *S1pr1*$^{\Delta GFAP}$ SVZ-NSCs group, indicating that these genes are specifically regulated by ApoM-S1P-S1PR1 signaling (Fig. 5b, c). Moreover, gene ontology (GO) analysis showed that the 324 DEGs were enriched in GO Biological Process gene sets related to cell proliferation (positive regulation of cell proliferation and positive regulation of gene expression) and pathways promoting cell growth (positive regulation of ERK1 and ERK2 cascade)

https://doi.org/10.1038/s41467-025-60750-0

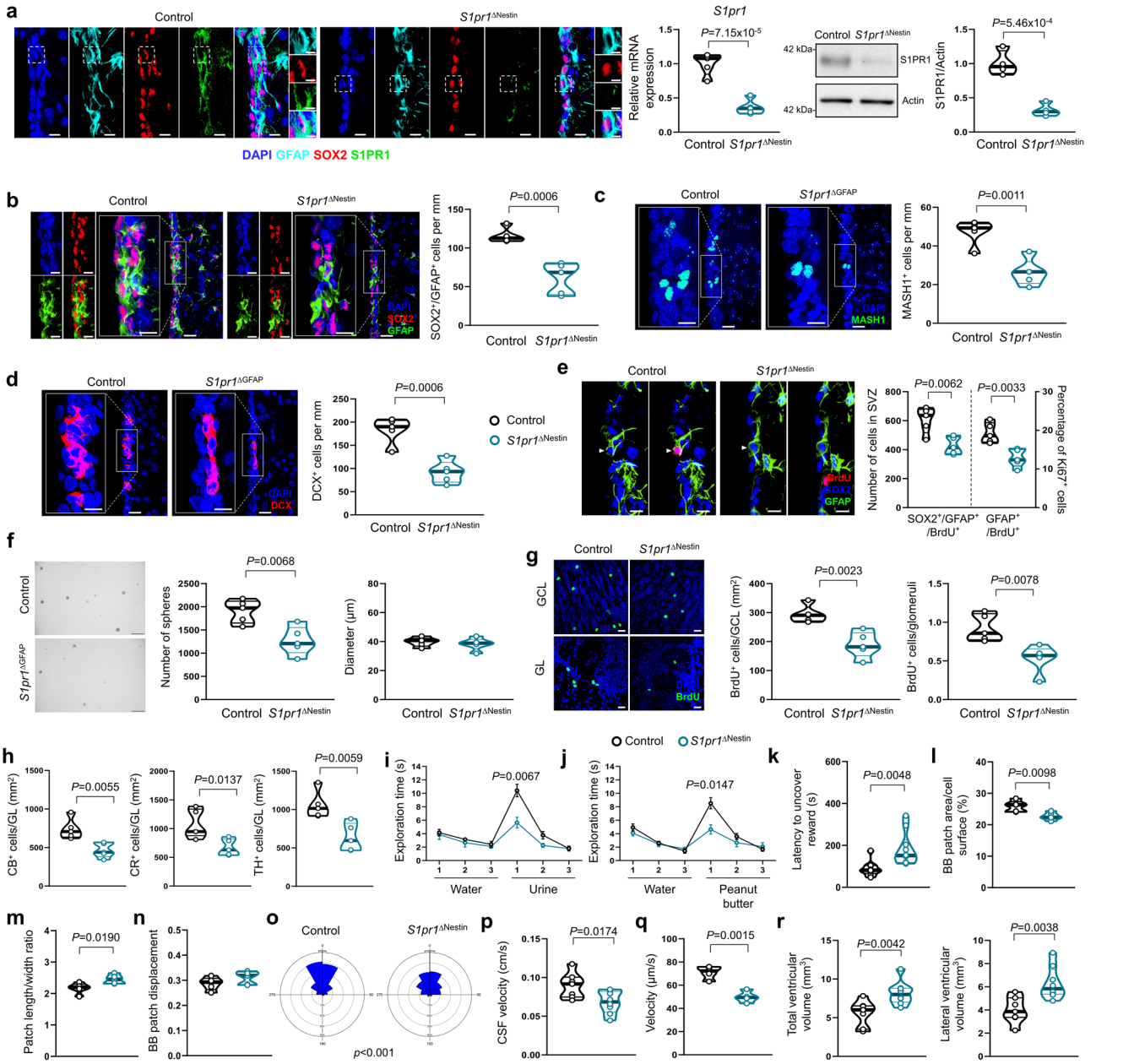

Fig. 4 | S1PR1 in the SVZ-NSCs is essential for maintaining neurogenesis and ependymal planar polarity. a Immunofluorescence images for S1PR1 (green), GFAP (cyan), SOX2 (red) and DAPI (blue) in the SVZ of control and *S1pr1*$^{\Delta Nestin}$ mice (left) with mRNA (middle; n = 5/group) and protein levels (right; n = 4/group) of S1PR1 in NSCs from control and *S1pr1*$^{\Delta Nestin}$ mice. Scale bars, 10 μm (enlarged, 5 μm). **b**–**d** Representative immunofluorescence images and quantification of SOX2$^+$GFAP$^+$ cells **(b)**, MASH1$^+$ cells **(c)**, and DCX$^+$ cells **(d)** in the SVZ (n = 5/group). Scale bars, 30 μm (enlarged, 15 μm). **e** Representative immunofluorescence images of SOX2$^+$GFAP$^+$BrdU$^+$ cells (left) and quantification of SOX2$^+$GFAP$^+$BrdU$^+$ cells and GFAP$^+$BrdU$^+$Ki67$^+$ cells (right) in the SVZ (n = 5/group). Scale bars, 10 μm**. f** Representative images (left), number (middle), and diameter (right) of primary neurospheres (n = 5/group). Scale bars, 300 μm. **g** Representative immunofluorescence images and quantification of BrdU$^+$ newly formed neurons in the GCL and GL in the OB (n = 5/group). Scale bars, 30 μm. **h** Quantification of CB$^+$ cells, CR$^+$ cells, TH$^+$ cells in GL (n = 5/group). **i, j** The results of olfactory habituation–dishabituation test for both urine **(i)** and peanut butter **(j)** scents (Control, n = 9; *S1pr1*$^{\Delta Nestin}$, n = 10). **k** The latency to locate a buried food reward (Control, n = 9; *S1pr1*$^{\Delta Nestin}$, n = 10). **l** Quantification of BB patch area in the walls of LV (n = 5/group). **m** Quantification of length/width ratios of the BB patches (n = 5/group). **n** Quantification of BB patch displacement (n = 5/group). **o** Angular distribution of BB patch angles in ependymal cells (Control, n = 296; *S1pr1*$^{\Delta Nestin}$, n = 291; five animals/group). **p** Quantification of CSF flow in the cerebral aqueduct (Control, n = 7; *S1pr1*$^{\Delta Nestin}$, n = 8). **q** Quantification of velocity of microbeads propelled by cilia at the surface (n = 4/group). **r** Quantification of total ventricle (left) and LV (right) volume (Control, n = 7; *S1pr1*$^{\Delta Nestin}$, n = 8). **a**–**h, k**–**n, p**-**r** Two-tailed student's t test. **i, j** Two-way ANOVA for repeated measures. **o** Two-sided Watson U^2 test. All error bars indicate s.e.m. All data analysis was done at 4-month-old mice. Source data are provided as a Source Data file.

(Fig. 5d). The ERK signaling pathway is known to play a crucial role in the proliferation of neural progenitor cells[47] and S1P is recognized for its ability to activate ERK involved in this signaling[48]. These previous reports suggested to us a pivotal mechanism through which ApoM-S1P-S1PR1 influences SVZ-NSC behavior by activating the ERK signaling pathway. As expected, ApoM$^+$HDL led to a significant increase in phosphorylated ERK levels in control SVZ-NSCs, but not in S1PR1 depleted SVZ-NSCs (Fig. 5e). Additionally, the phosphorylation of ERK induced by ApoM$^+$HDL was completely abolished by treatment with a S1PR1 antagonist (W146) or inhibitor of G protein-coupled receptors signaling (pertussis toxin, PTX) (Fig. 5e). The increased self-renewal of SVZ-NSCs induced by ApoM$^+$HDL was also inhibited by the application

https://doi.org/10.1038/s41467-025-60750-0

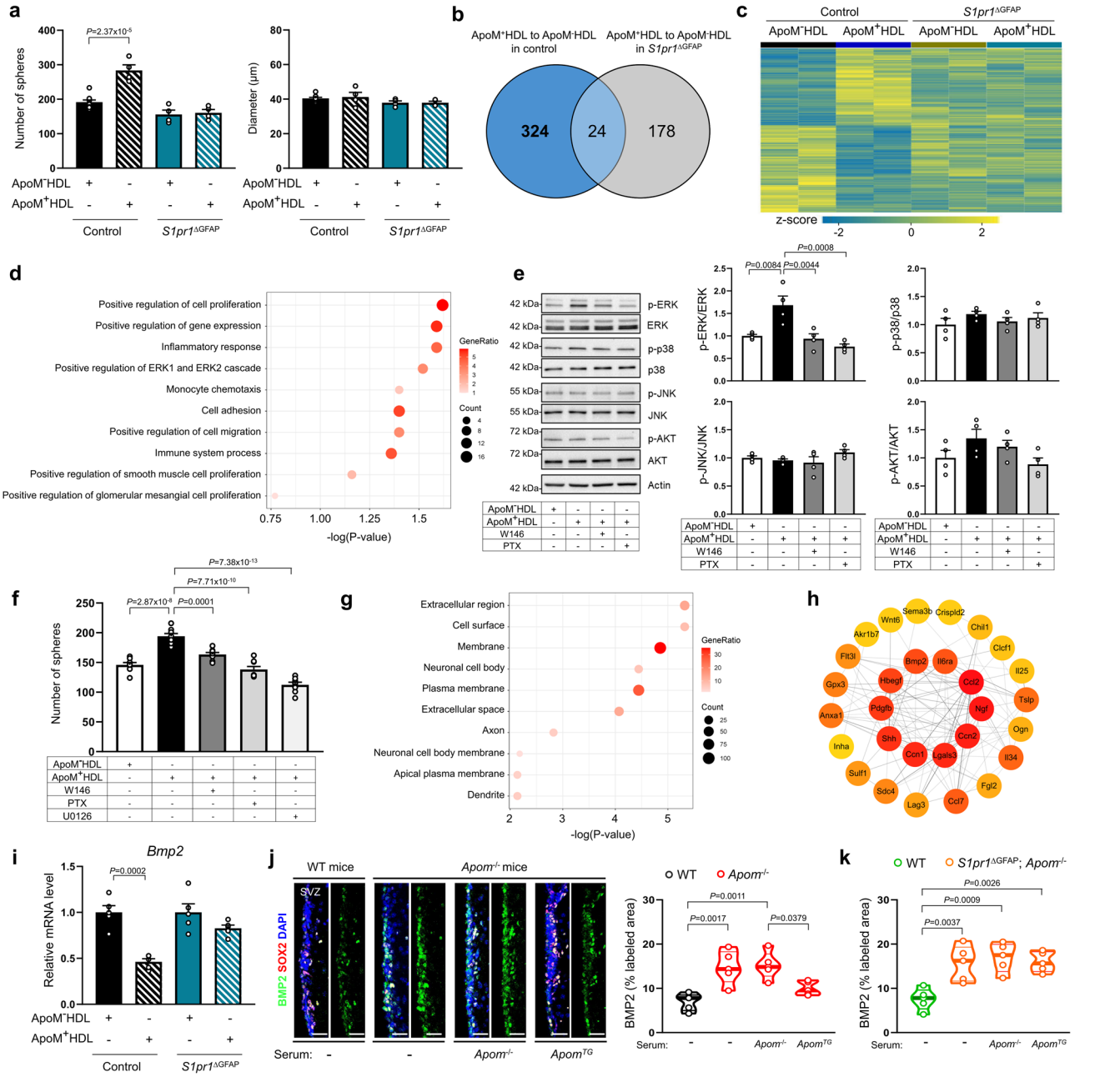

Fig. 5 | ApoM-S1P-S1PR1 signaling promotes SVZ-NSCs self-renewal via ERK pathway and inhibits BMP2 expression. a Quantification of the number and diameter of neurospheres after treatment with ApoM$^-$HDL and ApoM$^+$HDL in NSCs derived from wild-type SVZ (left to right, n = 9, 4, 4, 4). **b** A Venn diagram illustrating the DEGs of SVZ-NSCs in a comparison as indicated. **c** Heatmap of expression values for DEGs. **d** GO term enrichment analysis of biological process using DAVID Bioinformatics Resources 6.8. **e** Western blot analysis of p-ERK, p-p38, p-JNK, and p-AKT levels in SVZ-NSCs treated with ApoM$^+$HDL, including comparisons of pretreatment with or without W146, and PTX (n = 4/group). **f** Quantification of the number of neurospheres following treatment with ApoM$^+$HDL, with additional comparisons for pretreatment with or without W146, PTX, and U0126 (n = 8/group). **g** GO term enrichment analysis of cellular component using DAVID Bioinformatics Resources 6.8. **h** Hub genes identified from the PPI network using the Cytohubba plug in Cytosacpe. **i** mRNA levels of *BMP2* in SVZ-NSCs after treatment with ApoM$^-$HDL and ApoM$^+$HDL (n = 5/group). **j** Representative immunofluorescence images and quantification of BMP2 immunoreactivity in the SVZ of WT, *Apom*$^{-/-}$ and *Apom*$^{-/-}$ mice transplanted with *Apom*$^{-/-}$ or *Apom*^{TG} serum (n = 5/group). Scale bars, 30 μm. **k** Quantification of BMP2 immunoreactivity in the SVZ of WT, *S1pr1*$^{\Delta GFAP}$; *Apom*$^{-/-}$ mice and *S1pr1*$^{\Delta GFAP}$; *Apom*$^{-/-}$ mice transplanted with *Apom*$^{-/-}$ or *Apom*^{TG} serum (n = 5/group). **a, e, f, j, k** One-way analysis of variance, Tukey's post hoc test. **d, e** One-sided Fisher's exact test with Benjamini-Hochberg correction for multiple testing. **i** Two-tailed student's t test. All error bars indicate s.e.m. Source data are provided as a Source Data file.

of W146, PTX, or ERK pathway inhibitor (U0126) (Fig. 5f), indicating that the activation of ApoM-S1P-S1PR1 signaling in SVZ-NSCs regulates their self-renewal capacity through the ERK signaling pathway.

To further investigate the ependymal cell dysfunction caused by SVZ-NSCs deficient in ApoM-S1P-S1PR1 signaling, we further performed GO analysis for the 324 DEGs specifically influenced by ApoM-S1P-S1PR1 signaling and found that these genes were enriched in GO Cellular Component gene sets associated with extracellular region and space (Fig. 5g). Overall, these gene products are secreted by cells that remain within the interstitial fluid, impacting the local niche, and intriguingly, NSCs secrete a variety of substances known to modulate the V-SVZ neurogenic niche[49].

Based on these results and previous reports, we therefore hypothesized that secretory factors derived from SVZ-NSCs and regulated through ApoM-S1P-S1PR1 signaling could significantly influence the structural and functional integrity of ependymal cells. To assess this, we focused on identifying the hub genes within gene sets associated with the extracellular region. Hub gene analysis on the 38 DEGs associated with the extracellular region was performed to identify hub genes demonstrating significant connectivity within the gene network. This analysis was visualized using the Cytoscape plugin, cytoHubba, where genes positioned in the inner concentric circles indicate high connectivity, whereas genes in the outer concentric circles display lower connectivity (Fig. 5h). Among the top 10 hub genes (located in the inner concentric circles) identified, we found BMP2, which is previously reported to be specifically associated with ependymal ciliogenesis[50,51]. According to this finding, we confirmed BMP2 expression in control and S1PR1 deficient SVZ-NSCs with treatment of ApoM$^-$HDL or ApoM$^+$HDL. The result showed reduction of BMP2 expression in control SVZ-NSCs treated with ApoM$^+$HDL, but not in S1PR1 deficient SVZ-NSCs (Fig. 5i). In line with these observations, BMP2 expression was upregulated in the SVZ of *Apom*$^{-/-}$ mice and suppressed following the administration of *Apom*^{TG} serum in these mice, but not in *S1pr1*$^{\Delta GFAP}$ mice lacking ApoM (Fig. 5j, k). To evaluate the impact of BMP2 on the impairment of the structural and functional integrity of ependymal cells by the blood ApoM-S1P complex deficiency, we injected AAV-shRNA-Ctrl or AAV-shRNA-*Bmp2* into the cerebral ventricle of *Apom*$^{-/-}$ mice. Effective infection in vivo was confirmed by detecting virus-encoded eGFP and by performing anti-BMP2 immunofluorescence staining in the V-SVZ neurogenic niche (Supplementary Fig. 16a). The administration of AAV-shRNA-*Bmp2* resulted in the amelioration of the basal body polarity disruption in ependymal cells and enhanced CSF flow within the cerebral aqueduct, along with improved ciliary motility (Supplementary Fig. 16b–g). Consequently, this intervention effectively mitigated ventricular enlargement in *Apom*$^{-/-}$ mice (Supplementary Fig. 16h). Therefore, these data suggested that ApoM-S1P-S1PR1 signaling in healthy SVZ-NSCs inhibits BMP2 secretion, thereby maintaining the structural and functional integrity of ependymal cells.

The blood ApoM-S1P complex is deeply associated with early neuropathological features in AD

Extensive research has reported that olfactory dysfunction and ventricular enlargement are prevalent, early neuropathological features of PD and AD[23–25]. Moreover, decreased levels of circulating S1P have been observed in patients with AD and PD[52,53]. Based on these observations, we investigated the potential correlation between the blood ApoM-S1P complex and these early neuropathological features of PD and AD patients. In the case of PD patients, there were no significant changes in the levels of ApoM and S1P within HDL compared to healthy controls (Fig. 6a, b). However, ApoM and S1P were notably reduced in early-stage AD patients compared to control individuals (Fig. 6c, d). Further analysis revealed a significant correlation between HDL-S1P levels and the Cross-Cultural Smell Identification Test (CC-SIT) scores, which are widely used for the assessment of olfactory function. These results suggested that higher levels of HDL-S1P may be associated with better olfactory performance. Of note, most early AD patients exhibited low HDL-S1P levels and poor olfactory function (Fig. 6e). In addition, we found that HDL-S1P levels inversely correlated with measurements of ventricle size, especially in early AD patients with low HDL-S1P levels (Fig. 6f). These findings implied that the blood ApoM-S1P complex could be a potential diagnostic target for early neuropathological features in AD.

Based on the AD patient results, we investigated potential impairments of the V-SVZ neurogenic niche at young ages in APP/PS1 mice, which is a well-studied and validated AD mouse model[54,55]. Moreover, the therapeutic effect of blood ApoM-S1P complex was evaluated using APP/PS1/*Apom*^{TG} mice. Four-month-old APP/PS1 mice showed a reduction of ApoM and S1P levels in the plasma and HDL fraction (Fig. 7a and Supplementary Fig. 17a, b), while S1P levels were increased in those of APP/PS1/*Apom*^{TG} mice at the same age (Fig. 7a). Regarding the decrease of blood ApoM-S1P, young APP/PS1 mice exhibited a significant decrease in the SVZ-NSC pool (Fig. 7b–f), alongside notable impairments in olfactory bulb neurogenesis and olfactory function (Fig. 7g–k). Additionally, these mice displayed abnormalities in cilia polarity of ependymal cells, CSF circulation, and ventricular enlargement (Fig. 7l–q), closely paralleling the deficits observed in *Apom*$^{-/-}$ mice. Notably, these impairments of the V-SVZ neurogenic niche, olfaction, CSF flow, and enlarged ventricle were significantly restored by enhancing the blood ApoM-S1P complex as observed in APP/PS1/*Apom*^{TG} mice. Overall, these data highlighted the potential of elevating the blood ApoM-S1P complex for the treatment of early AD.

Emerging evidence has suggested that the presence of peripheral amyloid-beta (Aβ) can impair liver function[56,57], the primary site for ApoM production, indicating the possibility for peripheral Aβ to influence blood ApoM-S1P concentrations in AD. Based on this, we hypothesized that peripheral Aβ might lead to reduction of hepatic ApoM expression, thereby affecting the overall levels of HDL-bound ApoM-S1P complex in the blood of AD patients and mice. The results showed a reduction in both *Apom* mRNA and ApoM protein levels in the liver of young APP/PS1 mice compared to WT mice (Supplementary Fig. 17c, d). Further extending this observation in vitro, we exposed mouse and human hepatocytes to oligomeric Aβ. The treatment with oligomeric Aβ induced a decrease of ApoM expression in both mouse and human hepatocytes (Supplementary Fig. 17e–h). Collectively, these findings suggest that peripheral Aβ may contribute to reduced hepatic ApoM production, which in turn could lead to a reduction of the blood ApoM-S1P complex and potentially impair the V-SVZ neurogenic niche and early neuropathological features of AD.

Discussion

The importance of circulating blood factors has been widely investigated in the regulation of neurogenic niches. In particular, previous studies have demonstrated the positive or negative effects of circulating molecules on maintenance of hippocampal neurogenesis and cognitive function, suggesting their potential as therapeutic targets for age-related neurodegenerative diseases, such as AD[58–60]. Despite the fact that the V-SVZ is adjacent to the CSF-filled LV, which is abundant in various circulating factors, studies on the neurophysiological roles of these factors in the regulation of the V-SVZ neurogenic niche have been poorly investigated. Previously, S1P metabolism and S1PRs signaling were known to mediate the regulation of neurogenesis, the migration of new neurons, and the proper functioning of the olfactory bulb in the brain[61–64]. However, in this study, we revealed the more role of the ApoM-S1P complex as a circulating factor essential for maintaining the V-SVZ neurogenic niche. Our findings demonstrate that the blood ApoM-S1P complex efficiently accesses the SVZ and regulates SVZ neurogenesis through S1PR1 signaling in SVZ-NSCs. Beyond its role in the SVZ niche, the blood ApoM-S1P complex also appears to regulate S1P levels in the CP, a region with fenestrated capillaries similar to those in the SVZ, as well as in the CSF. While this study focused on its role in the SVZ, further investigation is required to define the function of blood ApoM−S1P complex in CP physiology and its broader relevance to CSF homeostasis. Furthermore, we showed that defects in this complex cause olfactory dysfunction and ventricular enlargement, known early pathological features of AD, through defective S1P1 receptor signaling in SVZ-NSCs (Supplementary Fig. 18). These findings may explain a pathological mechanism for the cause of early AD symptoms, while suggesting potential diagnostic or therapeutic targets for early AD.

Deficiency of the blood ApoM-S1P complex caused a decrease of the SVZ-NSC pool, neurogenesis, and ependymal cell polarity.

https://doi.org/10.1038/s41467-025-60750-0

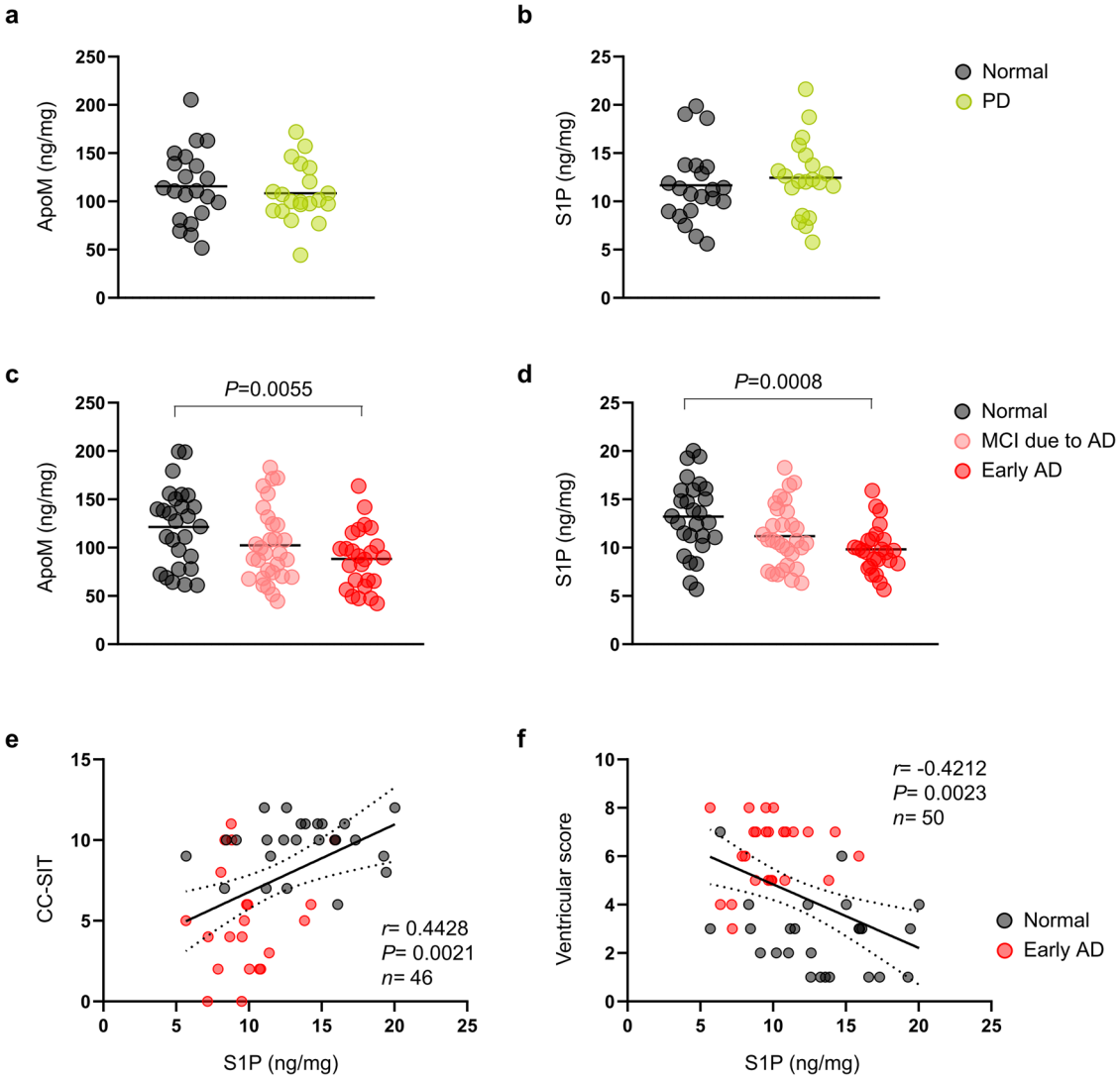

Fig. 6 | Decrease of blood ApoM-S1P complex correlates with olfactory dysfunction and LV enlargement in early AD patients. a, b Levels of ApoM (**a**) and S1P (**b**) within HDL from PD patients (Normal, $n = 21$; PD, $n = 20$). **c, d** Levels of ApoM (**c**) and S1P (**d**) within HDL from AD patients (Normal, $n = 27$; MCI due to AD, $n = 30$; Early AD, $n = 25$). **e** Correlation between S1P levels within HDL and CC-SIT scores (Normal, $n = 25$; Early AD, $n = 21$). Intercepts and 95 % confidence intervals are indicated in the graphs. **f** Correlation between S1P levels within HDL and ventricular scores (Normal, $n = 25$; Early AD, $n = 25$). Intercepts and 95 % confidence intervals are indicated in the graphs. **a, b** Two-tailed student's *t* test. **c, d** One-way analysis of variance, Tukey's post hoc test. **e, f** two-tailed simple linear regression; *r*, Pearson correlation coefficient. Source data are provided as a Source Data file.

Conversely, its enhancement restored these damages in the V-SVZ neurogenic niche through S1PR1, which is predominantly expressed in the NSCs. The activation of ApoM-S1P-S1PR1 signaling in NSCs notably improved ependymal cell damage, indicating the interaction between NSCs and ependymal cells in the V-SVZ neurogenic niche. Moreover, we found increased levels of the secretory signaling molecule BMP2 in the SVZ-NSCs in the absence of ApoM-S1P-S1PR1 signaling, and SVZ-specific reduction of BMP2 prevented impairment of ependymal cell polarity caused by blood ApoM-S1P deficiency in mice. These results were supported by previous research demonstrating that molecules derived from NSCs are essential for maintaining the structure of the SVZ niche, especially ependymal cells[65,66].

The impairment of the V-SVZ neurogenic niche by the blood ApoM-S1P complex deficiency led to olfactory dysfunction, CSF flow abnormalities, and LV enlargement. Moreover, we found that the level of blood ApoM-S1P is reduced in early AD patients and was deeply correlated with olfactory dysfunction and ventricular enlargement. Other groups have also confirmed lower S1P or ApoM levels in the plasma or CSF in AD[52,67] and reported that S1P signaling pathways are associated with LV volume[68]. While these findings suggest a potential association between the blood ApoM-S1P complex and early neuropathological features in AD, they do not establish causation. Further longitudinal studies are necessary to clarify whether reductions in ApoM-S1P levels play a causal role in these early features of AD. The neuropathological features associated with the blood ApoM-S1P complex deficiency are mainly observed in patients with normal pressure hydrocephalus (NPH)[69,70]. NPH is considered one of the leading risk factors for AD and many patients with NPH are known to develop AD[71,72]. Although the exact mechanism remains unclear, this is probably related to the fact that enlarged ventricles and reduced CSF clearance in NPH contributes to accumulation of neurotoxins such as Aβ and tau-protein. The continuous circulation and drainage of CSF, known as the glymphatic system, is responsible for clearance of metabolic waste, immune and neuronal function, and it could be affected by the vessel system in the brain[73,74]. Particularly, a decline in CSF drainage due to impairment of the vascular system leads to increase of Aβ deposits and memory dysfunction in AD[75,76]. Moreover,

https://doi.org/10.1038/s41467-025-60750-0

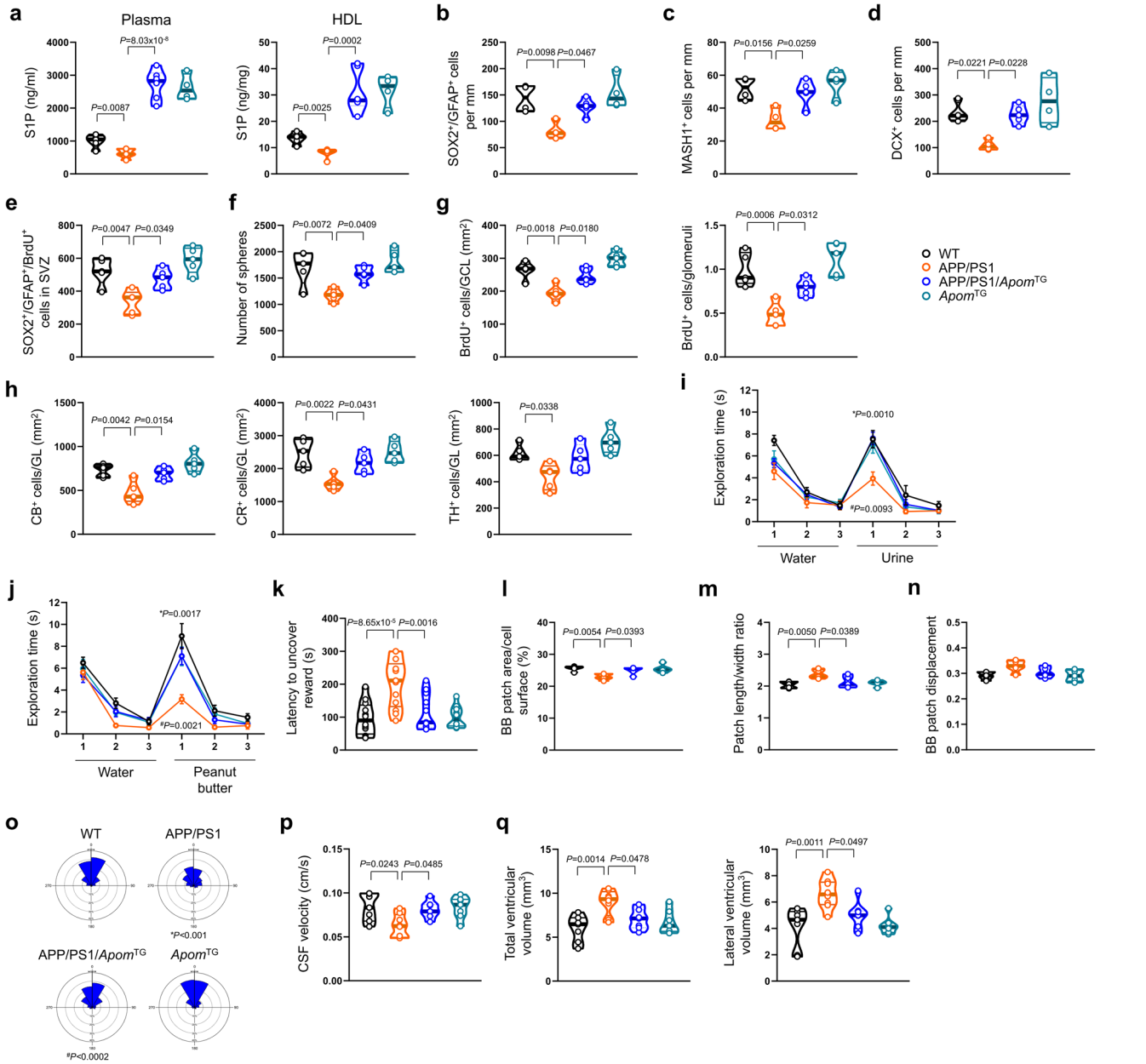

Fig. 7 | Enhancement of blood ApoM-S1P complex ameliorates early events in APP/PS1 mice. a S1P concentration (WT, $n = 5$; APP/PS1, $n = 5$; APP/PS1/*Apom*^{TG}, $n = 6$; *Apom*^{TG}, $n = 4$). **b**–**d** Quantification of SOX2$^+$GFAP$^+$ cells (b), MASH1$^+$ cells (c), and DCX$^+$ cells (d) in the SVZ (WT, $n = 4$; APP/PS1, $n = 4$; APP/PS1/*Apom*^{TG}, $n = 5$; *Apom*^{TG}, $n = 4$). **e** Quantification of SOX2$^+$GFAP$^+$BrdU$^+$ cells in the SVZ (n = 5/group). **f** The number of primary neurospheres (n = 5/group). **g** Quantification of BrdU$^+$ newly formed neurons in the GCL (left) and GL (right) in the OB (n = 5/group). **h** Quantification of CB$^+$ cells, CR$^+$ cells, TH$^+$ cells in GL (n = 5/group). **i, j** The results of olfactory habituation–dishabituation test for both urine **(i)** and peanut butter **(j)** scents (WT, $n = 11$; APP/PS1, $n = 13$; APP/PS1/*Apom*^{TG}, $n = 12$; *Apom*^{TG}, $n = 10$). $^{\#}P$: WT vs APP/PS1, $^{*}P$: APP/PS1 vs APP/PS1/*Apom*^{TG}. **k** The latency to locate a buried food reward (WT, $n = 12$; APP/PS1, $n = 13$; APP/PS1/*Apom*^{TG}, $n = 11$; *Apom*^{TG}, $n = 10$). **l** Quantification of BB patch area in the walls of LV ($n = 5$/group). **m** Quantification of BB patch length/width ratios (n = 5/group). **n** Quantification of BB patch displacement (n = 5/group). **o** Analysis of angular distribution of BB patch angles in ependymal cells (WT, $n = 289$; APP/PS1, $n = 314$; APP/PS1/*Apom*^{TG}, $n = 311$; *Apom*^{TG}, $n = 296$; five animals/group). $^{\#}P$: WT vs APP/PS1, $^{*}P$: APP/PS1 vs APP/PS1/*Apom*^{TG}. **p** Quantification of CSF flow in the cerebral aqueduct (WT, $n = 7$; APP/PS1, $n = 8$; APP/PS1/*Apom*^{TG}, $n = 7$; *Apom*^{TG} $n = 7$). **q** Quantification of total ventricle volume (m), LV volume (WT, $n = 7$; APP/PS1, $n = 8$; APP/PS1/*Apom*^{TG}, $n = 7$; *Apom*^{TG}, $n = 7$). **a** Two-tailed student's t test. **b**–**h, k, l, n, p, q** One-way analysis of variance, Tukey's post hoc test. **i, j** Two-way ANOVA for repeated measures. **m** Contingency table test. **o** Two-sided Watson U^2 test. All error bars indicate s.e.m. All data analysis was done at 4-month-old mice. Source data are provided as a Source Data file.

previous studies have demonstrated that S1P is involved in the activation of both vasorelaxation and vasoconstriction responses by regulating intracellular signal transduction pathways through S1PR1 expressed in vascular smooth muscle and endothelial cells[77,78]. These previous reports and our current data reveal the possibility that the blood ApoM-S1P complex may be essential for regulation of both circulation and drainage of CSF by maintaining homeostasis of the V-SVZ neurogenic niche and vascular system in the brain, and suggests that blood ApoM-S1P may be a link in the development of NPH into AD. Further studies, including investigating how deficiency of the blood ApoM-S1P complex affects pathologies such as Aβ accumulation and memory dysfunction in late-stage AD through the glymphatic system, could provide further insights into the role of this complex in neurodegenerative disease.

We are also aware that the APP/PS1 mice used in this study has limitations in perfectly reflecting the physiological conditions of AD

patients because changes in adult neurogenesis have been controversial in many AD mouse models with APP overexpression. However, many mouse models with APP overexpression commonly show impairments in adult neurogenesis within the SVZ[79,80], and it is well-documented that adult neurogenesis is reduced in the SVZ of AD patients[81]. The APP/PS1 mouse model we used also exhibited impaired adult SVZ neurogenesis as early as 4 months of age, suggesting that these models are effective for recapitulating the neurogenesis deficits observed in AD patients. The fact that the Aβ is predominantly produced in the brain under the normal physiological conditions raises the possibility of an artificial reduction in blood ApoM-S1P complex by peripheral Aβ in this AD mouse model. However, previous studies have reported that oligomeric Aβ effluxes from the brain into the blood, increasing blood oligomeric Aβ level in AD[82,83]. Moreover, since APP/PS1 mouse used in this study is a model in which APP is primarily overexpressed in brain neurons, brain-derived blood oligomeric Aβ may have a direct effect on the reduction of blood ApoM-S1P complex, demonstrating that this model may be suitable for replicating the issues of the reduction of blood ApoM-S1P complex caused by peripheral oligomeric Aβ observed in AD patients. Nonetheless, it is important to note that elevated peripheral Aβ levels in these mice may not be exclusively brain-derived, as the promoter used in this model also drives APP expression in non-neuronal cells. Therefore, further studies are required to specifically determine whether brain-derived Aβ contributes to the increase in peripheral Aβ levels and the subsequent reduction in the blood ApoM-S1P complex.

According to a recently updated AD drug development pipeline, most agents currently in clinical trials target late-stage AD symptoms such as the accumulation of Aβ or tau[84]. Thus, there remains an important need to develop prophylactic drugs that can prevent AD progression by impacting the early neuropathological features of this disease. Our results demonstrating the potential therapeutic effects of the blood ApoM-S1P complex provide a potential approach for treating these early symptoms that should be further investigated. Specifically, we showed that enhancement of the blood ApoM-S1P complex results in significant improvement of the damaged V-SVZ neurogenic niche, olfactory dysfunction, reduced CSF flow, and ventricular enlargement in early AD mice. In addition, our results suggest that S1PR1 agonists may be a promising agent for treatment of these early neuropathological features in AD and indicate that further development of these agonists to target the V-SVZ neurogenic niche and glymphatic pathway is warranted. We expect that our findings will serve as a basis for the future development of prophylactic agents for early AD, and stimulate further studies assessing the synergistic therapeutic effects of the blood ApoM-S1P complex or S1PR1 agonists with current therapeutic agents for improvement of neuropathological features in early and late-stage AD.

Methods

Mice

All animal experiments were performed in accordance with protocols approved by the Institutional Animal Care and Use Committee (IACUC) at Kyungpook National University (approval no. KNU 2023-0532). The following mouse lines were used: C57BL/6 wild type (WT) mice (The Jackson Laboratory), *Apom*$^{-/-}$ mice[26] (C57BL/6 background), *Apom*^{TG} mice[26] (C57BL/6 background), *Edg1*$^{eGFP/eGFP}$ knock-in mice (stock number 028623, The Jackson Laboratory), *Nestin*-creERT2 (stock number 016261, The Jackson Laboratory), *GFAP*-creERT2 (stock number 012849, The Jackson Laboratory), *Cdh5*-creERT2 (stock number 13073, Taconic Biosciences), and *S1pr1*$^{loxP/loxP}$ mice (stock number 019141, The Jackson Laboratory). To generate a specific deletion of *S1pr1* in GFAP-positive cells[85] or brain endothelial cells, *GFAP*-creERT2 mice or *Cdh5*-creERT2 mice were bred to *S1pr1*$^{loxP/loxP}$ mice, and tamoxifen (100 mg kg^{-1}) was intraperitoneally administered at postnatal day 30 for 5 days. S1PR1-GFP signaling reporter mice were previously described[41]. Briefly, B6N.129S6(FVB)-S1pr1$^{tm3.1(tTA,-Arrb2)Rlp/J}$ mice (stock number 026275, Jackson Laboratory) were crossed with pTRE-H2BGFP mice (stock number 005104, Jackson Laboratory) for the generation of a mouse carrying a S1PR1 knock-in with the tetracycline-regulated transactivator (tTA)-tobacco etch virus (TEV) protease recognition sequence (tevs) fusion protein and an Arrb2 (murine β-arrestin)-TEV protease fusion protein, and the transgene expressing the human histone 1 (H2BJ) protein and GFP fusion protein under the control of a tetracycline responsive promoter element. Mice expressing one allele of both transgenes were considered S1PR1-GFP reporter mice. Littermates expressing only the H2BJ-GFP allele without the S1PR1 knock-in were used as controls. Transgenic mouse lines overexpressing the hAPP695swe (APP) and presenilin-1M146V (PS1) mutations were originated from GlaxoSmithKline (Harlow, UK)[55] and maintained as described previously[54]. *Apom*^{TG} mice were bred with APP/PS1 mice to generate APP/PS1/*Apom*^{TG} mice. We used littermate mice that were sex- and age-matched between experimental groups. Both male and female mice were used for all experiments. The block randomization method was used to allocate the animals to experimental groups. To eliminate the bias, all investigators were blinded to the experimental groups and analysis such as data collection and data analysis. Mice were housed at a 12 h day/12 h night cycle, 21–22 °C, and 50–60 % humidity with free access to water and food pellets. Experimental mice were euthanized by induction of deep anesthesia via intraperitoneal injection of ketamine (100 mg kg^{-1}) and xylazine (10 mg kg^{-1}), followed by rapid brain dissection or transcardial perfusion. For mice with undesirable genotypes, euthanasia was performed by carbon dioxide (CO_2) asphyxiation followed by cervical dislocation.

Mouse plasma or serum collection

Mouse blood was collected into sodium heparin-coated tubes via intracardial bleed at the time of death. Plasma was generated by centrifugation (15,493 × *g*, 4 °C, 5 min) of freshly collected blood, and aliquots were stored at -80 °C until use. To collect serum, mouse blood was collected in an e-tube and the blood was allowed to clot by leaving it undisturbed at room temperature for 30 min. Serum was collected by centrifugation (15,493 × *g*, 4 °C, 5 min) and aliquots were stored at -80 °C until use.

Human plasma collection

The experimental protocols for the human study were reviewed and approved by the Institutional Review Board (IRB) of Hanyang University Hospital (IRB no. HYUH 2016-12-029-003). Informed consent was obtained from all subjects in accordance with the ethics committee guidelines of Hanyang University. Patients enrolled in this study were diagnosed with AD or PD according to established clinical criteria and were consecutively recruited to minimize self-selection bias. Age-matched healthy controls were recruited from volunteers. Human plasma samples were collected from both men and women with AD and PD, along with age-matched healthy controls without AD or PD, at Hanyang University Hospital (Supplementary Table 1). The sex of the participants was determined based on self-report.

LC-MS/MS for S1P quantification

A 50 µl aliquot of the samples was mixed with 75 µl of methanol containing 10 ng ml^{-1} of S1P-d7 (internal standard, IS) for 5 min. After centrifugation at 16,000 × *g* for 5 min, Supernatants (100 µl each) were transferred to autosampler vials and 10 µl aliquots were injected into an Agilent 6470 Triple Quadrupole LC-MS/MS system (Agilent, Wilmington, DE) coupled with an Agilent 1260 HPLC system. Separation was performed on a Synergy Polar RP column (4 µm particle size, 2.0 mm×150 mm, Phenomenex) using a gradient elution of distilled water containing 0.1 % formic acid (A) and methanol containing 0.1 % formic acid (B) at a flow rate of 0.2 ml min^{-1}. The gradient elution program was as follows: 0 – 6.0 min 20 % A and 80 % B, 6.0 – 6.5 min

transition from 20 % A and 80 % B to 10 % A and 90 % B, 6.5 – 12.5 min 10 % A and 90 % B, 12.5 – 13.0 min transition from 10 % A and 90 % B to 20 % A and 80 %, and 13.0 – 23.5 min 20 % A and 80 % B. Calibration standard solutions were prepared by evaporating 50 µl of a stock solution of S1P and reconstituted with the same volume of phosphate buffered solution (PBS). The final concentrations of S1P were 0.1, 0.5, 1, 2, 5, 50, and 100 ng ml^{-1}. A 75 µl aliquot of S1P-d7 (IS) was added to 50 µl of calibration standard, mixed vigorously for 5 min, and centrifuged at 16,000 g for 5 min. Aliquots (10 µl) of supernatants were injected into the LC-MS/MS system. Quantification was carried out using multiple reaction monitoring (MRM) at m/z 380.3 → 264.2 for S1P and m/z 387.2 → 271.2 for S1P-d7 (IS) in positive ionization mode and collision energy of 20 eV. The lower limit of quantification was determined to be 0.1 ng ml^{-1} and linearity was observed in the standard range of 0.1–100 ng ml^{-1}.

Pharmacokinetics of stable isotope-labeled ApoM-S1P complex

To prepare the stable isotope-labeled ApoM-S1P complex, we utilized the ability of erythrocytes to efficiently synthesize S1P from exogenous sphingosine and export it to $ApoM^+HDL$[86–88]. For this purpose, mouse blood was drawn into K3-EDTA vials and centrifuged for 10 min at 573 × g at room temperature. Plasma and buffy coat were discarded, and erythrocytes were pooled. These erythrocytes were mixed with Buffer A (20 mM HEPES, 3.3 mM NaH_2PO_4, 2.9 mM KCl, 1 mM $MgCl_2$, 138 mM NaCl, 1 mg ml^{-1} glucose, pH 7.4) containing 100 µM stable isotope-labeled sphingosine (sphingosine-d7, Avanti, 860657 P) and incubated for 60 min at room temperature with end-over-end rotation. After incubation, erythrocytes were centrifuged for 10 min at 573 × *g*, washed twice with 200 µl of Buffer A, and incubated with $ApoM^+HDL$ for another 60 min at room temperature with end-over-end rotation. Stable isotope-labeled S1P bound $ApoM^+HDL$ was then extensively dialyzed against PBS at 4 °C to remove unbound components. C57BL/6 mice were administered a 0.5 mg kg^{-1} intravenous dose of a stable isotope-labeled ApoM-S1P complex. Venous blood samples were collected at 1, 4, 8, and 24 h post-administration. Plasma was then separated from whole blood via centrifugation and subsequently stored at -80 °C for further analysis. Simultaneously, brain tissues were also collected at these time points, rinsed thoroughly with physiological saline, weighed, and processed into 20 % tissue homogenates by homogenizing with four volumes of saline. For biochemical assays, 50 µl aliquots of both plasma and tissue homogenates were deproteinized using 250 µl of methanol containing 50 ng ml^{-1} spinganibe-1-phosphate-d7 (SPA-1-P-d7) (IS). After centrifuging at 16,000 × *g* for 5 min, 120 µl of the supernatant was transferred into autosampler vials. Analysis was conducted by injecting 10 µl aliquots into an Agilent 6470 Triple Quadrupole LC-MS/MS system, which was coupled with an Agilent 1260 HPLC system (Agilent Technologies, Wilmington, DE). Separation was performed on a Synergy Polar RP column (4 µm particle size, 2.0 mm×150 mm, Phenomenex) using a gradient elution of distilled water containing 0.1 % formic acid (A) and methanol containing 0.1 % formic acid (B) at a flow rate of 0.2 ml min^{-1}. The gradient elution program was as follows: 0 – 6.0 min 35 % A and 65 % B, 6.0 – 6.5 min transition from 35 % A and 65 % B to 10 % A and 90 % B, 6.5 – 12.5 min 10 % A and 90 % B, 12.5 – 13.0 min transition from 10 % A and 90 % B to 35 % A and 65 %, and 13.0 – 23.5 min 35 % A and 65 % B. Calibration standard solutions were prepared by evaporating 50 µl of a stock solution of S1P and reconstituted with the same volume of plasma and 20 % brain homogenates, respectively. The final concentrations of S1P-d7 and sphingosine-d7 were 1, 5, 20, 100, 500, and 2000 ng ml^{-1} and 0.05, 0.1, 0.5, 1, 5, 20, and 50 ng ml^{-1}, respectively. A 250 µl aliquot of SPA-1-P-d7 (IS) was added to 50 µl of calibration standard, mixed vigorously for 5 min, and centrifuged at 16,000 g for 5 min. Aliquots (10 µl) of supernatants were injected into the LC-MS/MS system. Quantification was carried out using multiple reaction monitoring (MRM) at m/z 387.2 → 271.2 for S1P-d7, m/z 307.3 → 271.2 for sphingosine-d7, and 389.2 → 273.2 for SPA-1-P-d7 (IS) in positive ionization mode and collision energy of 20 eV. The lower limit of quantification was determined to be 1 ng ml^{-1} for S1P-d7 and 0.05 ng ml^{-1} for sphingosine-d7 and linearity was observed in the standard range of 1 – 5,000 ng ml^{-1} for S1P-d7 and 0.05 - 200 ng ml^{-1} for sphingosine-d7.

BrdU administration

For BrdU labeling, 100 mg kg^{-1} of BrdU (Sigma-Aldrich, B5002) was injected into 3-month-old mice intraperitoneally once a day for 5 days. Brains were collected when the mice were 4 months old.

Histological analysis

For immunofluorescence staining, brain was cut on a vibratome (30 µm). The following antibodies were used: SOX2 (Goat, 1:500, R&D system, AF2018), GFAP (Chicken, 1:500, Abcam, ab4674), MASH1 (Rabbit, 1:1000, Abcam, ab213151), DCX (Rabbit, 1:400, Abcam, ab18723), BrdU (Rat, 1:400, Abcam, ab6326), Ki67 (Rabbit, 1:1000, Abcam, ab15580), Cleaved Caspase-3 (Rabbit, 1:200, Cell Signaling Technology, 9664S), NeuN (Chicken, 1:2500, Genetex, GTX00837), CB (Mouse, 1:5000, Swant, CB300), CR (Rabbit, 1:2000, Swant, CR7697), TH (Rabbit, 1:200, Milipore, MAB5280), Acetylated Tubulin (Mouse, 1:1000, Sigma-Aldrich, T7451), S100β (Rabbit, 1:200, Abcam, ab52642), Nestin (Mouse, 1:100, Milipore, MAB353), BMP2 (Rabbit, 1:200, Abcam, ab14933), CD31 (Goat, 1:40, R&D system, AF3628), S1P1/EDG1 (Rabbit, 1:100, Santa cruz, SC-25489), and BLBP (Rabbit, 1:300, Millipore, ABN14). All were visualized using Alexa Fluor 488, 594, or 633 conjugated anti-rabbit, -rat, -mouse, - chicken, or -goat IgG antibodies (All at 1:1000, Thermo Fisher Scientific). The sections were analyzed with a laser-scanning confocal microscope (FV3000; Olympus) or with a BX51 microscope (Olympus). The number of $SOX2^+GFAP^+$, $MASH1^+$, and DCX^+ cells in SVZ was determined within the first three cell layers adjacent to the ependyma and normalized to the length of the ventricle, as previously reported[89–92]. Some other markers were assessed by examining the entire SVZ in each section. All $GFAP^+SOX2^+BrdU^+$, $GFAP^+BrdU^+Ki67^+$, $Caspase\text{-}3^+$, and $TUNEL^+$ cells were evaluated and recorded in every three coronal vibratome sections. Immunostaining of the SVZ was analyzed in the regions shown in Supplementary Fig. 19. To estimate the total number of cells positive for specific markers in the DG, cells exhibiting immunopositivity were counted within the granule cell layer and the subgranular layer of the DG in every sixth coronal vibratome section throughout the hippocampus. MetaMorph software (Molecular Devices) and ImageJ software (National Institutes of Health) were used for quantification. The quantification of the area of the LV was performed as previously reported, with minor modifications[93]. For each animal, three sections (between -0.1 and 0.1 mm from the bregma) that was stained with 4′,6-diamidino-2-phenylindole (DAPI) were averaged and used for quantification. The quantification of the volume of the LV was performed as previously reported[94]. Every fifth coronal section (between 0 and 1.2 mm from the bregma) that was stained with DAPI was used for measurements. The volume of the lateral ventricles was approximated using the equation $V = T \cdot \sum Area(LV)$, where T is the distance between sections and Area(LV) denotes the areas of the LV in each section. Immunoreactivity was assessed within a defined quantification area measuring 200 µm × 10 µm located in the SVZ. For hematoxylin and eosin (H&E) staining, the procedure was carried out using the H&E staining kit (Vector laboratories, H-3502) following the manufacturer's provided instructions.

TUNEL staining

Cell death was detected by the In Situ Cell Death Detection Kit, TMR red (Roche, 12156792910). Analysis was performed according to the manufacturer's protocol.

Whole-mount immunostaining

For isolating the LV in whole-mount staining[95], the brain was removed from the skull and whole mounts of the LV walls were freshly dissected.

First, dissect the olfactory bulbs away from the brain, then make a perpendicular cut through the midbrain, using the mesencephalic tectum as a guide. Next, divide the brain along the interhemispheric fissure. Open the tissue following the corpus callosum line, separating the hippocampus, septum, and diencephalon from the cortex. This will expose the LV walls. The exposed walls were then fixed overnight at 4 °C in 4 % paraformaldehyde (PFA) in 0.1 % Triton X-100 in 0.1 M phosphate buffer saline pH 7.4 (PBS). After washing off the PFA, the wholemount specimens are incubated for 1 hour at room temperature in a blocking solution composed of 10 % normal goat serum and 0.5 % Triton X-100 in PBS. The whole-mount samples were incubated in primary antibodies in blocking solution, including γ-tubulin (Mouse, 1:1000, Sigma-Aldrich, T6557) and anti-β-catenin (Rabbit, 1:400, Cell Signaling Technology, 9562S); for 24 h at 4 °C. Secondary antibodies, Alexa Fluor 488-conjugated anti-mouse and Alexa Fluor 594-conjugated anti-rabbit, were diluted at a ratio of 1:500 and incubated at room temperature for 2 h. For wholemount choroid plexus, the LV choroid plexus was dissected and incubated in 4 % PFA at room temperature for 5 min., and then immunostained as described above. Confocal images were acquired by an Olympus FV3000 microscope with a field size of 120 μm x 120 μm. The BB displacement was calculated as the distance between the cell center and the BB patch center divided by the distance from the cell center to the membrane[34]. To examine a cell's BB patch angle, a vector was drawn from the cell center to the BB patch center and the angle deviation was compared using Two-sided Watson's 2-sample U2 test. The distance and vector angles were measured using ImageJ software (National Institutes of Health).

Scanning electron microscopy

Mice were perfused with a solution containing 2 % PFA and 2.5 % glutaraldehyde in PBS. Their brains were then immersed in the same buffer for 2 h at room temperature. The LV walls were isolated under a dissecting microscope. Subsequently, the specimens underwent post-fixation in 1 % osmium tetroxide for 1 h three times and in 1 % thiocarbohydrazide for 20 min twice, employing the OTOTO technique[96]. Following this, the specimens were dehydrated in a gradient ethanol series, critical-point dried using CO_2, and finally coated in palladium. Then, the samples were viewed under a field-emission scanning electron microscopy (Hitachi, SU8220). The orientation of ciliary tufts was manually measured in 15 ~ 30 tufts from each animal.

CSF Flow

For the quantification of CSF flow in the cerebral aqueduct[97], five averages of nine axial slices were acquired using a FLOWMAP phase contrast sequence. The slices were centered at the anatomical image volume and matched the field of view and in-plane resolution of the anatomical images, with a slice thickness of 0.5 mm, TE = 9.1 ms, TR = 30 ms, and flip angle = 10°. Velocity mapping with flow encoding in slice direction was used with a velocity encoding coefficient of 0.2 cm s^{-1}, directed away from the cerebellum. The total scan time was 10 min.

Magnetic resonance imaging

The animal MRI study was performed using a horizontal bore 9.4 T/30 cm MR scanner (Bruker BioSpec, Billerica, MA, USA). A mouse head volume coil (Bruker BioSpin) was used. Animals were anesthetized and maintained with 1.5–2 % isoflurane during the experiments. T2-weighted images were acquired for volume measurements (Repetition time/Echo time = 4400/30 ms, field of view = 15 × 15 mm, matrix = 256 × 256, number of averages = 6, thickness = 0.3 mm, scan time = 11 min). Quantitative analysis of the volume of ventricular systems, based on acquired MR images, was conducted using the open-source software 3D Slicer[98]. For measurements of cortical thickness, three measurements were taken for each animal in both hemispheres, specifically within the area corresponding to the primary somatosensory cortex barrel field (S1BF). These measurements were conducted using three evenly spaced MRI sections, chosen at approximate bregma levels of +0.60 mm, -0.60 mm, and -1.8 mm.

The ventricular score measurement. The ventricular size in each individual were assessed on a semiquantitative 10-point scale (grades of 0-9)[99]. Ventricular grades extended from slitlike ventricles (grade 0) to markedly enlarged ventricles (grade 9). All images were read by board-certified radiologists with at least 1 year of neuroradiology fellowship training.

Video microscopy analysis of ependymal ciliary function

Fresh brains were dissected from animals[92]. 300 μm-thick coronal sections from LV walls were obtained and transferred to a 35-mm glass microwell dish in DMEM at 37 °C. Before video microscopy analysis, a small amount of polystyrene beads (Invitrogen, 2 μm) was added and mixed with the medium. Bead movement was recorded with a Leica Thunder DMi8 microscope. Images were captured at 16.1 frames per second, and the mean velocity of each tracked microbead was calculated using ImageJ software (National Institutes of Health).

Treatment of mice with serum, ApoM-HDL, or ApoM$^+$HDL

Two-month-old *Apom*$^{-/-}$ mice were intravenously injected with either 50 μl of serum from WT, *Apom*$^{-/-}$, or *Apom*^{TG} mice. In some experiments, 150 μg of ApoM$^-$HDL or ApoM$^+$HDL was injected through the tail vein of *Apom*$^{-/-}$ mice[100]. This procedure was performed twice a week for a duration of 8 weeks.

Cerebral ventricular injection

For the assessment of CSF circulation, Evans Blue dye was used[92]. In brief, after anesthesia, Evans Blue dye (5 μl, 4 % in PBS) was injected into the right LV at a rate of 5 μl min^{-1} using stereotaxic coordinates of +0.3 mm anterior, +1 mm lateral, and −2.3 mm dorsal relative to the bregma. Five minutes post-injection, the mice were sacrificed, and their brains were fixed in 4 % PFA overnight. Subsequently, the brains were sectioned into 1-mm-thick slices for analysis. For the in vivo viral injections, 1-month-old *Apom*$^{-/-}$ mice underwent intraventricular injection with 5 μl of AAV carrying a plasmid that encodes for a small hairpin RNA targeting *Bmp2* for knockdown, driven by the U6 promoter (AAV-shRNA-*Bmp2*). As a control, a scramble sequence (AAV-shRNA-Ctrl) was used. The injections were precisely administered using stereotaxic coordinates: +0.3 mm anterior, ±1 mm lateral, and −2.3 mm dorsal relative to the bregma.

Western blotting

Samples were lysed in RIPA buffer (Cell Signaling Technology, 9806), then subjected to SDS-PAGE and transferred to a nitrocellulose membrane. Membranes were blocked with 5 % milk, incubated with primary antibody and then incubated with the appropriate horseradish peroxidase-conjugated secondary antibody[54]. Primary antibodies to the following proteins were used: S1P1/EDG1 (Rabbit, 1:1000, Santa cruz, SC-25489), ERK (Rabbit, 1:1000, Cell Signaling Technology, 4695S), p-ERK (Rabbit, 1:1000, Cell Signaling Technology, 9101S), P38 (Rabbit, 1:1000, Cell Signaling Technology, 8690S), p-P38 (Rabbit, 1:1000, Cell Signaling Technology, 4511S), JNK (Rabbit, 1:1000, Cell Signaling Technology, 9252S), p-JNK (Rabbit, 1:1000, Cell Signaling Technology, 4668S), AKT (Rabbit, 1:1000, Cell Signaling Technology, 4691S), p-AKT (Rabbit, 1:2000, Cell Signaling Technology, 4060S), ApoM (Rabbit, 1:1000, Genetex, GTX33015), ApoM (Rabbit, LSBio, LS-C298172), and β-Actin (1:1000, Santa cruz, SC-47778). Rabbit-HRP (1:1000, Cell Signaling Technology, 7074) and mouse-HRP (1:1000, Cell Signaling Technology, 7076) were used as secondary antibody. We performed densitometric quantification using the ImageJ software (National Institutes of Health). Images have been cropped for presentation.

ELISA

For measurement of human ApoM, we used commercially available ELISA kits (NOVUS, NBP2-69839). ELISA was then performed according to the manufacturer's instructions. Mouse ApoM levels were determined using in-house developed sandwich ELISAs. Briefly, rabbit polyclonal anti-ApoM (0.5 μg ml^{-1}, Genetex, GTX33015) in ELISA coating buffer (Abcam, ab210899) was coated onto MaxiSorp ELISA plates (Thermo Fisher Scientific) overnight at 4 °C. Plates were washed twice wash buffer (Abcam, ab206977) and blocked for 2 h at room temperature with blocking buffer (Abcam, ab210904). The plates were washed twice, diluted plasma and standard ApoM protein (LSBio, LS-G14868) in blocking buffer were incubated for 2 h at RT. Following washing with wash buffer, biotin-conjugated rabbit polyclonal anti-ApoM (2 μg ml^{-1}, LSBio, LS-C300462) in blocking buffer was added and incubated for 1 h at RT. After standard washing, wells were further incubated with streptavidin-HRP (1:1000, Abcam, ab210901) in blocking buffer for 1 h at RT and results were developed with TMB substrate (Abcam, ab210902). Absorbance was measured at 450 nm using a Varioskan LUX Multimode Microplate Reader (Thermo Fisher Scientific).

Isolation and separation of HDL

HDL (1.063 <d < 1.21 g l^{-1}) were isolated by ultracentrifugation of plasma with a S140-AT rotor and a micro ultracentrifuge (Hitachi, CS150NX)[101]. The density was adjusted with NaBr (Sigma-Aldrich, 310506). Ultracentrifugation was performed at 317,700 × *g* at 4 °C for 16 h (d = 1.063 g l^{-1}) or 24 h (d = 1.21 g l^{-1}). The purified HDL were dialyzed extensively against PBS at 4 °C and stored at −80 °C. Mouse total HDL isolated by ultracentrifugation was processed through an anti-ApoM affinity column to separate ApoM-containing from ApoM-depleted HDL. A polyclonal anti-ApoM antibody (Genetex, GTX33015) was bound to HiTrap NHS-activated columns (Cytiva) at 0.5 mg ml^{-1} gel, as per the manufacturer's instructions. After applying the HDL solutions to the columns, the elution was collected, and the flow-through was rerun through the column to ensure complete binding. $ApoM^{+}$HDL was subsequently eluted with 0.1 M glycine at a pH of 2.2. This anti-ApoM chromatography was repeated until all ApoM particles were removed, resulting in the preparation of ApoM-depleted HDL ($ApoM^{-}$HDL).

Olfactory habituation-dishabituation test. For the olfactory habituation–dishabituation test[31,89], two distinct odors were sequentially presented: water and peanut butter (10% w/v in water), or water paired with urine samples from an unfamiliar mouse. For each odor (or water), three consecutive trials are conducted, lasting 2 min per trial, with a 1 min intertrial interval. A fresh odor sample (1 μl) is presented to each mouse on filter paper, which is then enclosed within a small perforated Petri dish. Presentations occurred in a clean, standard mouse cage. Prior to the presentations, animals were habituated for 30 min in this cage. The cumulative sniffing time was manually recorded during each odor presentation. Sniffing was scored when the animal was oriented towards the dish with its nose within 2 cm or closer to the dish.

Olfactory avoidance test. For the olfactory avoidance test[31,102,103], animals were habituated for 1 h in a clean, standard mouse cage prior to the experiments. In the trial, mice were transferred to a test cage where a filter paper scented with three different volumes (0.1, 1, and 10 μl) of nTMT (Sigma-Aldrich, 219185) was introduced. During the 10 min test period, avoidance times were recorded. Avoidance time refers to the duration spent in the section of the test cage not containing the nTMT-scented filter paper, when the cage was divided into two equal areas. The time spent in the section without the nTMT scent was measured using equipment and Time OFCR1 software from O'hara & Co. Avoidance behavior was quantified using an avoidance index calculated as follows: avoidance index = (P - 50) / 50, where P represents the percentage of avoidance time during the 10 min test period.

Odor discrimination test

For the odor discrimination test[31,103,104], mice were food-restricted to maintain them at 80-85 % of their free-feeding body weights and were trained over a period of 4 days to associate one of the two related odorants with a sugar reward. During the training period, mice underwent four 10 min trials daily: two trials involved the presentation of a 2MB (Sigma-Aldrich, 193070) odor paired with a sugar reward, and two trials involved the presentation of a CB (Sigma-Aldrich, C95609) odor, unpaired with any sugar reward. On days 5 to 7, mice underwent three different tests. On day 5, the two test odorants were placed separately under the bedding without any sugar reward on each side of the cage (Test 1). On day 6, only the 2MB odorant was placed under the bedding without sugar on one side of the cage (Test 2). On day 7, only the CB odorant was placed under the bedding without sugar on one side of the cage (Test 3). Behaviors were captured using a digital video camera to measure the duration that mice spent digging for each odorant during the 5 min test period. 20 μl of 2MB and CB were used in each odorant presentation. Discrimination between odors was measured using a discrimination index defined as (digging time for 2MB - digging time for CB)/(digging time for 2MB + digging time for CB) during test 1.

Buried food test

For the buried food test[105], mice were acclimated to the food reward (M&M Minis) by placing two samples in their home cage overnight for two days prior to the behavioral test. Mice underwent three 10 min habituation sessions over three consecutive days, during which one piece of the food reward was placed on top of the bedding in the center of the arena. Before testing, mice were fasted in their home cages for 18 h. During a test session, mice were subjected to three consecutive trials with 1 h intervals to locate a quarter piece of an M&M mini, which was pseudorandomly hidden beneath the bedding in one of five approximate locations (four corners or center). Immediately after being placed in the arena, the latency to find the buried food was measured. The average of these three trials was used as the latency score.

Morris water maze test

To assess spatial memory performance, the Morris water maze task was conducted[54]. The apparatus consisted of a circular white tank (1.0 m in diameter, 30 cm in height) filled with water (22–24 °C) to a depth of 20 cm. White, opaque, non-toxic paint was added to obscure the platform from view. A circular platform (10 cm in diameter) was submerged 6–8 mm below the water surface and remained in a fixed location throughout the training for each mouse. Platform positions were counterbalanced across experimental groups. One day prior to training, mice were habituated to the maze. The animals were subjected to four trials per day. A training session consisted of a series of four trials per day for 10 consecutive days (a total 40 trials). In each trial, mice were placed into the water at one of four randomly assigned, equally spaced starting positions. Each mouse was allowed 60 seconds to locate the hidden platform. If the mouse failed to locate the platform within this time, it was gently guided to it. The latency to reach the platform was recorded for each trial. After reaching the platform, mice remained there for 10 seconds before being returned to their home cage. On day 11, a probe trial was conducted with the platform removed. Mice were introduced into the maze from a designated start quadrant and allowed to swim freely for 60 seconds.

Fear conditioning test

For fear conditioning[54], mice were individually placed into the conditioning chamber on the conditioning day. After a 60 s exploratory period, a tone (10 kHz, 70 dB) was delivered for 10 s; this served as the conditioned stimulus (CS). The CS co-terminated with the

unconditioned stimulus (US), a scrambled electrical footshock (0.3 mA, 1 s). The CS-US pairing was delivered twice at a 20 s intertrial interval. On day 2, each mouse was placed in the fear-conditioning chamber containing the same exact context, but with no administration of a CS or foot shock. Freezing was analyzed for 5 min. On day 3, a mouse was placed in a test chamber that was different from the conditioning chamber. After a 60 s exploratory period, the tone was presented for 60 s without the foot shock. The rate of freezing response of mice was used to measure the fear memory.

The open field test

The open field test was used for locomotion and anxious behaviors[54]. The open field box consisted of a square box. Each animal was placed in the box for 10 min. Overall activity in the box was measured, and the amount of time and distance traveled in the center arena was noted. After each trial, the test chambers were cleaned with a damp towel and distilled water followed by 70 % alcohol.

The light-dark test

The light-dark test was used for assessing the anxiety-like behavior[54]. One chamber was brightly illuminated, whereas the other chamber was dark. Mice were placed into the dark chamber and allowed to move freely between the two chambers.

Neurosphere culture and formation assay

Primary neurosphere cultures were prepared from 4-month-old mice[27,106]. First, brains were dissected and the SVZ isolated in EBSS (Gibco, 24010043). Tissues were transferred to EBSS containing 0.9 mg ml^{-1} papain (Worthington, LS003120), 0.2 mg ml^{-1} L-cysteine (Sigma-Aldrich, C6852), 0.5 mM EDTA (Invitrogen, 15575020), and incubated for 20 min at 37 °C. Tissue was transferred to DMEM/F12 (Gibco, 11330032) and carefully triturated with a fire-polished Pasteur pipette to a single-cell suspension. Isolated cells were collected by centrifugation, resuspended in DMEM/F12 medium containing 2 % B-27 (Gibco, 17504044), 500 U ml^{-1} penicillin-streptomycin (Gibco, 15070063), 20 ng ml^{-1} epidermal growth factor (R&D system, 2028-EG), and 20 ng ml^{-1} fibroblast growth factor (R&D system, 3139-FB-025/CF) and seed in a 48-well plate adding 500 μl (25,000 viable cells/500 μl) to each well. Cells were incubated at 37 °C with 5 % CO_2. In this culture system, the primary culture typically presents as a layer of dead cells with clearly distinguishable floating neurospheres. It is important to collect all primary spheres without disturbing the attached cells. Cells were passaged every 6 days by enzymatic dissociation with TrypLE Select (Gibco, 12563011) at 37 °C for 7 min. The purity of the isolated NSCs was assessed through immunohistological analysis of SOX2 and Nestin immunoreactivity. The proportion of SOX2/Nestin-positive cells relative to all DAPI-positive cells was quantified to determine NSC purity, revealing that the cultures exhibited >99% purity (Supplementary Fig. 20a). For neurosphere formation assays, neurospheres were treated with TrypLE Select for 7 min, mechanically dissociated to a single-cell suspension, and replated in a 96-well plate, with each well receiving 200 μl of the suspension at low density (2.5 cells $μl^{-1}$) in growth medium[106]. Neurospheres were allowed to develop for 5 days in a 95 % air-5 % CO_2 humidified atmosphere at 37 °C. When indicated, neurosphere cultures were treated with $ApoM^+$HDL (10 μg ml^{-1}), $ApoM^-$HDL (10 μg ml^{-1}), IgG Isotype control antibody (50 μg ml^{-1}, R&D system, MAB002) or anti-S1P antibody (50 μg ml^{-1}, Echelon, Z-P300) at the time of plating. To neutralize S1P, $ApoM^+$HDL was pre-incubated with either the anti-S1P antibody or the IgG Isotype control antibody at a temperature of 37 °C for 1 h before use in the cultures. W146 (10 μM, TOCRIS, 3620), PTX (300 ng ml^{-1}, List Biological Laboratories, 180), and U0126 (10 μM, Sigma-Aldrich, 662005) were added into culture medium for 3 h before the addition of $ApoM^+$HDL. Neurosphere formation and diameter were analyzed after 5 days of incubation at 37 °C and 5 % CO_2.

Primary astrocyte culture

Primary astrocyte cultures were prepared from 4-month-old mice as previously described, with minor modifications[107,108]. First, brains were dissected, and the SVZ was isolated using EBSS (Gibco, 24010043). Tissues were then transferred to an EBSS solution containing 0.9 mg ml^{-1} papain (Worthington, LS003120), 0.2 mg ml^{-1} L-cysteine (Sigma-Aldrich, C6852), and 0.5 mM EDTA (Invitrogen, 15575020), and incubated for 20 minutes at 37 °C. Following incubation, tissues were transferred to DMEM/F12 (Gibco, 11320074) and gently dissociated to a single-cell suspension using a fire-polished Pasteur pipette. The cell suspension was centrifuged to collect cells, which were then resuspended in astrocyte medium composed of DMEM/F12 supplemented with 2 mM L-glutamine (Gibco, 25030-024), 0.6 % glucose (Sigma-Aldrich, G7021), 9.6 g ml^{-1} putrescine (Sigma-Aldrich, P7505), 6.3 ng ml^{-1} progesterone (Sigma-Aldrich, P6149), 5.2 ng ml^{-1} sodium selenite (Sigma-Aldrich, S5261), 0.025 mg ml^{-1} insulin (Wako, 099-06473), 0.1 mg ml^{-1} transferrin (Sigma-Aldrich, T2252), and 10 % FBS. The cells were seeded onto Matrigel-coated wells and cultured at 37 °C in 5 % CO_2. Astrocytes reached confluence approximately 6 days later, with medium changes every 2 days. To remove proliferating cells, oligodendrocyte progenitors, and neurons, the flasks were shaken at 100 rotations per minute for 3 hours at 22 °C. The purity of the isolated astrocytes was assessed through immunohistological analysis of GFAP and S100β immunoreactivity. The proportion of GFAP- or S100β-positive cells relative to all DAPI-positive cells was quantified to determine astrocyte purity, revealing that the cultures exhibited >93% purity.

Primary brain endothelial cell culture

Primary brain endothelial cells were isolated from 4-month-old mice[46]. First, brains were dissected to isolate the SVZ, which was then homogenized using a Dounce homogenizer. The homogenate was then centrifuged at 2000 *g* for 7 minutes, and the resulting pellet was resuspended in an 18% dextran solution (mol wt 60,000–90,000; USB, 14495) in DMEM/F12 (Sigma-Aldrich, D6421). This mixture was centrifuged at 7840 × *g* for 10 minutes. The supernatant containing myelin debris was discarded, and the pellet was resuspended in DMEM/F12 supplemented with 1 mg ml^{-1} collagenase/dispase (Roche, 10269638001), 40 μg ml^{-1} DNase I (Roche, 10104159001), and 0.147 μg ml^{-1} tosyllysine chloromethyl ketone (Sigma-Aldrich, T7254). The suspension was incubated at 37 °C for 75 minutes with occasional agitation to dissociate endothelial cells from pericytes, perivascular macrophages, and basement membrane remnants. Following another centrifugation at 2000 *g* for 7 minutes, the supernatant was discarded, and the cells were washed and seeded onto 6-well plates coated with mouse collagen IV (BD, 354233). The cultures were grown in DMEM/F12 enriched with 20 % fetal bovine serum (GIBCO, 16000036), 2 mM l-glutamine, 100 IU ml^{-1} penicillin, 100 μg ml^{-1} streptomycin, 0.25 μg ml^{-1} amphotericin B (Sigma-Aldrich, A5955), 100 U ml^{-1} heparin (Sigma-Aldrich, H3149), and 30 μg ml^{-1} endothelial cell growth supplement (Sigma-Aldrich, E0760). To selectively remove nonendothelial cells, 4 μg ml^{-1} puromycin (Sigma-Aldrich, P8833) was added for the initial 48 h post-preparation. The cultures were maintained at 37 °C in a 5 % CO_2 atmosphere, with medium changes every two days, until the cells reached confluence. The purity of the isolated endothelial cells was assessed through immunohistological analysis of CD31 immunoreactivity. The proportion of CD31-positive cells relative to all DAPI-positive cells was quantified to determine endothelial cell purity, revealing that the cultures exhibited >96% purity.

RNA isolation and real-time PCR analysis

RNA was extracted from the brain homogenates and cell lysates using the RNeasy Lipid Tissue Mini kit and RNeasy Plus Mini kit (QIAGEN) according to the manufacturer's instructions. cDNA was synthesized

from 5 µg of total RNA using a commercially available kit (Takara Bio Inc.). Quantitative real-time PCR was performed using the Thermal Cycler Dice Real Time System III (Takara). Used primers are described in Supplementary Table 2.

Digital PCR analysis

cDNA (1 ng) and specific primers were combined with 1x Absolute Q DNA Digital PCR Master Mix (Thermo Fisher Scientific, A52490) to achieve a total reaction volume of 10 µl. 9 µl of this mixture was subsequently loaded onto a QuantStudio MAP16 Digital PCR Plate (Thermo Fisher Scientific, A52688), and 15 µl of QuantStudio Absolute Q Isolation Buffer (Thermo Fisher Scientific, A52730) was overlayed in each well. Digital PCR was performed using the Applied Biosystems QuantStudio Absolute Q Digital PCR System (Thermo Fisher Scientific). Details of the primer utilized are provided in Supplementary Table 2.

Lentivirus Production and cerebroventricular injections. NSC-specific Split-cre was achieved by splitting the Cre-recombinase into two fragments and fusing them to the dimerizing GCN4 coiled-coil domain yielding the N-terminal NCre (hGFAP-NCre) and the C-terminal CCre fragment (Prominin-P2-CCre)[42,109]. Because two different promoters control the expression of the two Cre fragments, only NSCs coexpressing the two markers have functional Cre-recombinase. Lentiviral plasmids, which are consistent with 106-FUV-P2-CCre containing the C-terminal portion of Cre under the Prominin-P2 (CD133) promoter and 109-FUV-hGFAP-NCre containing the N-terminal portion of Cre (fused to GCN4) under the human GFAP promoter, were kindly provided from Prof. Dr. Magdalena Götz (University of Munich, Germany). 106-FUV-P2-CCre and 109-FUV-hGFAP-NCre were transfected in 293 T cells for production. Virus-containing media were collected, filtered, and concentrated by ultracentrifugation at 50,000 × *g* for 2 h and re-suspended in PBS. Viral titers were measured by serial dilution on 293 T cells, followed by flow cytometry analysis 48 h later. The titer of the virus used ranged between 2 and 5 × 10^9 plaque-forming units per ml. For injection, 2-month-old mice were anaesthetised and underwent surgery for implantation of a guide cannula into its brain. In brief, after anesthesia, a stainless steel cannula was implanted in the LV (+ 0.3 mm anterial, ± 1 mm lateral, −2.3 mm dorsal relative to bregma) using a stereotaxic frame. Split-cre plasmid a 1/1.5 CCre/NCre vector ratio was used as previously described[42]. Mice were daily injected with 3 µl of Split-cre virus containing solution into the LV for 8 weeks. As the control groups in each experiment, 3 µl of negative control vector were implanted.

RNA sequencing

Total RNA was isolated from NSCs of control and *S1pr1*$^{\Delta GFAP}$ mice treated with ApoM$^+$HDL or ApoM$^-$HDL using the Trizol reagent (Invitrogen, 15596026). To verify the size of PCR enriched fragments, we check the template size distribution by running on an Agilent Technologies 2100 Bioanalyzer using a DNA 1000 chip (Agilent Technologies). To assess the integrity of the total RNA, samples are run on the TapeStation RNA screentape (Agilent Technologies). A library was independently prepared with 0.5 µg of total RNA for each sample by Illumina TruSeq Stranded Total RNA Library Prep Gold Kit (Illumina, Inc). The libraries were quantified using KAPA Library Quantification kits for Illumina Sequencing platforms according to the qPCR Quantification Protocol Guide (KAPA BIOSYSTEMS) and qualified using the TapeStation D1000 ScreenTape (Agilent Technologies). Indexed libraries were then submitted to an Illumina NovaSeq6000 (Illumina), and paired-end sequencing reads were generated on the Illumina sequencing NovaSeq platform. The cleaned reads were aligned to the *Mus musculus (mm10)* using HISAT v2.1.0, based on the HISAT and Bowtie2 implementations. The reference genome sequence and gene annotation data were downloaded from NCBI Genome assembly and NCBI RefSeq database, respectively. Aligned data (SAM file format) were sorted and indexed using SAMtools v 1.9. After alignment, the transcripts were assembled and quantified using StringTie v2.1.3b. Gene-level and Transcript-level quantification were calculated as raw read count, FPKM (Fragments Per Kilobase of transcript per Million mapped reads) and TPM (Transcripts Per Million). Statistical analyses of differential gene expression were performed by edgeR exactTest using raw counts as input. In the QC step, genes with non-zero counts in all replicates at least one period group were selected. Filtered data set was applied with TMM normalization to correct the variation of library sizes among samples. Fold change and p-value were extracted from the result of exactTest. All p-values are adjusted by Benjamini-Hochberg algorithm to control false discovery rate. Significant gene list was filtered by fold change ≥ 2 or ≤ 0.5, *p*-value < 0.05 in comparisons between the two groups. Functional gene classification was performed by DAVID, with significance for GO terms defined as a Benjamini-corrected p-value. To identify hub genes, the Cytoscape plug-in CytoHubba was utilized to rank and examine significant nodes within the protein-protein interaction (PPI) network modules[110].

Olfactory assessment

Odor identification ability was evaluated with the CC-SIT[111], which consists of 12 microencapsulated odorants affixed to test cards. Participants were directed to scratch the card to release the scent, sniff it, and then choose one option from four given examples. The total score was derived from the count of accurately identified odors.

Preparation of brain microvessels

For brain microvessels preparation[112], brains were collected, and the meninges, choroid plexuses, brainstem, and cerebellum were carefully removed from the cerebrum. Subsequently, the SVZ was microdissected, rinsed, and homogenized using a loose-fit Dounce tissue grinder. The tissues were rinsed and homogenized using a loose-fit Dounce tissue grinder. The homogenates were centrifuged at 1000 × *g* for 5 minutes. The resulting pellet was resuspended in 18 % (w/v) dextran solution and centrifuged at 4400 × *g* for 15 minutes. The pellet (brain vessel) was resuspended in Hank's Balanced Salt Solution (HBSS) and passed through a 40 µm cell strainer. The unfiltered microvessels were washed with HBSS and collected by transferring them into a low-binding tube using HBSS. The brain microvessels were then lysed in ice-cold lysis buffer, sonicated, and centrifuged at 20,000 × *g*for 20 minutes, after which the supernatant was collected for western blot analysis.

Hepatocyte culture and treatments

AML-12 mouse hepatocytes (ATCC, CRL-2254) were cultured in DMEM containing 10 % FBS and 50 U ml^{-1} penicillin-streptomycin, following the instructions provided by ATCC. Cryopreserved primary human hepatocytes (iXCells Biotechnologies, 10HU-233) along with the Human Hepatocyte Culture Kit (iXCells Biotechnologies, MD-0111) were purchased and cultured according to the manufacturer's instructions. For the in vitro treatment, Aβ1-42 (Invitrogen, 03-112) was aggregated for 24 h at 37 °C. AML-12 mouse hepatocytes and primary human hepatocytes were plated in 6-well plates and, following an overnight incubation, were subjected to treatment with Aβ (10 µM). 36 h after the Aβ treatment, both AML-12 mouse hepatocytes and primary human hepatocytes were collected for analysis using real-time PCR and Western blot.

Statistical analysis

Sample sizes were determined by the G-Power software (ver 3.1.9.4, with α = 0.05 and power of 0.8). In general, statistical methods were not used to recalculate or predetermine sample sizes. Variance was

similar within comparable experimental groups. Individuals performing the experiments were blinded to the identity of experimental groups until the end of data collection and analysis for at least one of the independent experiments. All data are representative of at least three independent experiments. Comparisons between two groups were performed with a two-tailed student's t test. In cases where more than two groups were compared to each other, one-way analysis of variance (ANOVA) was used, followed by Tukey's HSD test. For circular statistics analyses, the two-sided Watson U^2 test was employed using Oriana software. Classical statistical analyses were performed using GraphPad Prism 8.0 software. $P < 0.05$ were considered as statistically significant.

Reporting summary

Further information on research design is available in the Nature Portfolio Reporting Summary linked to this article.

Data availability

All data supporting the findings of this study are available in the article and its supplementary information. Source data are provided with this paper as a Source Data file. All sequencing data generated in this study have been deposited in the National Center for Biotechnology Information Gene Expression Omnibus (GEO) and are accessible through the GEO Series accession number GSE268304. All remaining data can be found in the Article, Supplementary and Source Data files. Source data are provided with this paper.

References

1. Skoura, A. & Hla, T. Lysophospholipid receptors in vertebrate development, physiology, and pathology. *J. Lipid Res* **50**, S293–S298 (2009).
2. Liu, Z. et al. Sphingosine 1-phosphate stimulates insulin secretion and improves cell survival by blocking voltage-dependent K(+) Channels in β Cells. *Front Pharm*. **12**, 683674 (2021).
3. Czubowicz, K., Jęśko, H., Wencel, P., Lukiw, W. J. & Strosznajder, R. P. The role of ceramide and sphingosine-1-phosphate in Alzheimer's disease and other neurodegenerative disorders. *Mol. Neurobiol.* **56**, 5436–5455 (2019).
4. Aoki, S. et al. Sphingosine 1-phosphate-related metabolism in the blood vessel. *J. Biochem* **138**, 47–55 (2005).
5. Xu, N. & Dahlbäck, B. A novel human apolipoprotein (apoM). *J. Biol. Chem*. **274**, 31286–31290 (1999).
6. Blaho, V. A. et al. HDL-bound sphingosine-1-phosphate restrains lymphopoiesis and neuroinflammation. *Nature* **523**, 342–346 (2015).
7. Del Gaudio, I. et al. Endothelial Spns2 and ApoM Regulation of Vascular Tone and Hypertension Via Sphingosine-1-Phosphate. *J. Am. Heart Assoc.* **10**, e021261 (2021).
8. Christoffersen, C. et al. Endothelium-protective sphingosine-1-phosphate provided by HDL-associated apolipoprotein M. *Proc. Natl Acad. Sci. USA* **108**, 9613–9618 (2011).
9. Lagace, D. C. et al. Dynamic contribution of nestin-expressing stem cells to adult neurogenesis. *J. Neurosci.* **27**, 12623–12629 (2007).
10. Adam, Y. & Mizrahi, A. Long-term imaging reveals dynamic changes in the neuronal composition of the glomerular layer. *J. Neurosci.* **31**, 7967–7973 (2011).
11. Gheusi, G. et al. Importance of newly generated neurons in the adult olfactory bulb for odor discrimination. *Proc. Natl Acad. Sci. USA* **97**, 1823–1828 (2000).
12. Mouret, A., Lepousez, G., Gras, J., Gabellec, M. M. & Lledo, P. M. Turnover of newborn olfactory bulb neurons optimizes olfaction. *J. Neurosci.* **29**, 12302–12314 (2009).
13. Lim, D. A. & Alvarez-Buylla, A. The Adult Ventricular-Subventricular Zone (V-SVZ) and Olfactory Bulb (OB) Neurogenesis. *Cold Spring Harb. Perspect. Biol.* **8**, a018820 (2016).
14. Kumar, V. et al. The regulatory roles of motile cilia in CSF circulation and hydrocephalus. *Fluids Barriers CNS* **18**, 31 (2021).
15. Shen, Q. et al. Adult SVZ stem cells lie in a vascular niche: a quantitative analysis of niche cell-cell interactions. *Cell Stem Cell* **3**, 289–300 (2008).
16. Tavazoie, M. et al. A specialized vascular niche for adult neural stem cells. *Cell Stem Cell* **3**, 279–288 (2008).
17. Storer, M. A. et al. Interleukin-6 Regulates Adult Neural Stem Cell Numbers during Normal and Abnormal Post-natal Development. *Stem Cell Rep.* **10**, 1464–1480 (2018).
18. Delgado, A. C. et al. Endothelial NT-3 delivered by vasculature and CSF promotes quiescence of subependymal neural stem cells through nitric oxide induction. *Neuron* **83**, 572–585 (2014).
19. Ferrón, S. R. et al. Differential genomic imprinting regulates paracrine and autocrine roles of IGF2 in mouse adult neurogenesis. *Nat. Commun.* **6**, 8265 (2015).
20. Hamilton, L. K. et al. Aberrant Lipid Metabolism in the Forebrain Niche Suppresses Adult Neural Stem Cell Proliferation in an Animal Model of Alzheimer's Disease. *Cell Stem Cell* **17**, 397–411 (2015).
21. Höglinger, G. U. et al. Dopamine depletion impairs precursor cell proliferation in Parkinson disease. *Nat. Neurosci.* **7**, 726–735 (2004).
22. Nelles, D. G. & Hazrati, L. N. Ependymal cells and neurodegenerative disease: outcomes of compromised ependymal barrier function. *Brain Commun.* **4**, fcac288 (2022).
23. Nestor, S. M. et al. Ventricular enlargement as a possible measure of Alzheimer's disease progression validated using the Alzheimer's disease neuroimaging initiative database. *Brain* **131**, 2443–2454 (2008).
24. Dalaker, T. O. et al. Ventricular enlargement and mild cognitive impairment in early Parkinson's disease. *Mov. Disord.* **26**, 297–301 (2011).
25. Mesholam, R. I., Moberg, P. J., Mahr, R. N. & Doty, R. L. Olfaction in neurodegenerative disease: a meta-analysis of olfactory functioning in Alzheimer's and Parkinson's diseases. *Arch. Neurol.* **55**, 84–90 (1998).
26. Christoffersen, C. et al. Effect of apolipoprotein M on high density lipoprotein metabolism and atherosclerosis in low density lipoprotein receptor knock-out mice. *J. Biol. Chem.* **283**, 1839–1847 (2008).
27. Ferron, S. R. et al. A combined ex/in vivo assay to detect effects of exogenously added factors in neural stem cells. *Nat. Protoc.* **2**, 849–859 (2007).
28. Imayoshi, I. et al. Roles of continuous neurogenesis in the structural and functional integrity of the adult forebrain. *Nat. Neurosci.* **11**, 1153–1161 (2008).
29. Parrish-Aungst, S., Shipley, M. T., Erdelyi, F., Szabo, G. & Puche, A. C. Quantitative analysis of neuronal diversity in the mouse olfactory bulb. *J. Comp. Neurol.* **501**, 825–836 (2007).
30. Brill, M. S. et al. Adult generation of glutamatergic olfactory bulb interneurons. *Nat. Neurosci.* **12**, 1524–1533 (2009).
31. Kobayakawa, K. et al. Innate versus learned odour processing in the mouse olfactory bulb. *Nature* **450**, 503–508 (2007).
32. Mirzadeh, Z., Merkle, F. T., Soriano-Navarro, M., Garcia-Verdugo, J. M. & Alvarez-Buylla, A. Neural stem cells confer unique pinwheel architecture to the ventricular surface in neurogenic regions of the adult brain. *Cell Stem Cell* **3**, 265–278 (2008).
33. Doetsch, F., García-Verdugo, J. M. & Alvarez-Buylla, A. Regeneration of a germinal layer in the adult mammalian brain. *Proc. Natl Acad. Sci. USA* **96**, 11619–11624 (1999).
34. Boutin, C. et al. A dual role for planar cell polarity genes in ciliated cells. *Proc. Natl Acad. Sci. USA* **111**, E3129–E3138 (2014).
35. Guirao, B. et al. Coupling between hydrodynamic forces and planar cell polarity orients mammalian motile cilia. *Nat. Cell Biol.* **12**, 341–350 (2010).

36. Young, C. C. et al. Ependymal ciliary dysfunction and reactive astrocytosis in a reorganized subventricular zone after stroke. *Cereb. Cortex* **23**, 647–659 (2013).
37. Banizs, B. et al. Dysfunctional cilia lead to altered ependyma and choroid plexus function, and result in the formation of hydrocephalus. *Development* **132**, 5329–5339 (2005).
38. Kimura, T. et al. Role of scavenger receptor class B type I and sphingosine 1-phosphate receptors in high density lipoprotein-induced inhibition of adhesion molecule expression in endothelial cells. *J. Biol. Chem.* **281**, 37457–37467 (2006).
39. Argraves, K. M. & Argraves, W. S. HDL serves as a S1P signaling platform mediating a multitude of cardiovascular effects. *J. Lipid Res* **48**, 2325–2333 (2007).
40. Cahalan, S. M. et al. Actions of a picomolar short-acting $S1P_1$ agonist in $S1P_1$-eGFP knock-in mice. *Nat. Chem. Biol.* **7**, 254–256 (2011).
41. Kono, M. et al. Sphingosine-1-phosphate receptor 1 reporter mice reveal receptor activation sites in vivo. *J. Clin. Invest* **124**, 2076–2086 (2014).
42. Beckervordersandforth, R. et al. In vivo fate mapping and expression analysis reveals molecular hallmarks of prospectively isolated adult neural stem cells. *Cell Stem Cell* **7**, 744–758 (2010).
43. Park, M. H. et al. Characterization of the Subventricular-Thalamo-Cortical Circuit in the NP-C Mouse Brain, and New Insights Regarding Treatment. *Mol. Ther.* **27**, 1507–1526 (2019).
44. Yanagida, K. et al. Size-selective opening of the blood-brain barrier by targeting endothelial sphingosine 1-phosphate receptor 1. *Proc. Natl Acad. Sci. USA* **114**, 4531–4536 (2017).
45. Ridder, D. A. et al. TAK1 in brain endothelial cells mediates fever and lethargy. *J. Exp. Med* **208**, 2615–2623 (2011).
46. Park, M. H. et al. Vascular and Neurogenic Rejuvenation in Aging Mice by Modulation of ASM. *Neuron* **100**, 167–182.e169 (2018).
47. Learish, R. D., Bruss, M. D. & Haak-Frendscho, M. Inhibition of mitogen-activated protein kinase kinase blocks proliferation of neural progenitor cells. *Brain Res Dev. Brain Res* **122**, 97–109 (2000).
48. Harada, J., Foley, M., Moskowitz, M. A. & Waeber, C. Sphingosine-1-phosphate induces proliferation and morphological changes of neural progenitor cells. *J. Neurochem* **88**, 1026–1039 (2004).
49. Dause, T. J., Denninger, J. K., Smith, B. M. & Kirby, E. D. The neural stem cell secretome across neurodevelopment. *Exp. Neurol.* **355**, 114142 (2022).
50. Hiraoka, K., Inada, H., Yanai, K. & Osumi, N. Bone Morphogenetic Proteins Inhibit Ciliogenesis of Ependymal Cells in Vitro. *Tohoku J. Exp. Med* **252**, 199–208 (2020).
51. Hirao, T. et al. Transforming Growth Factor-β1 and Bone Morphogenetic Protein-2 Inhibit Differentiation into Mature Ependymal Multiciliated Cells. *Biol. Pharm. Bull.* **46**, 111–122 (2023).
52. Chua, X. Y. et al. Immunomodulatory sphingosine-1-phosphates as plasma biomarkers of Alzheimer's disease and vascular cognitive impairment. *Alzheimers Res Ther.* **12**, 122 (2020).
53. Schwedhelm, E. et al. Sphingosine-1-Phosphate, Motor Severity, and Progression in Parkinson's Disease (MARK-PD). *Mov. Disord.* **36**, 2178–2182 (2021).
54. Park, M. H., et al. Discovery of a dual-action small molecule that improves neuropathological features of Alzheimer's disease mice. *Proc. Natl Acad. Sci. USA* **119**, e2115082119 (2022).
55. Howlett, D. R. et al. Cognitive correlates of Abeta deposition in male and female mice bearing amyloid precursor protein and presenilin-1 mutant transgenes. *Brain Res* **1017**, 130–136 (2004).
56. Xu, Z. et al. The role of peripheral β-amyloid in insulin resistance, insulin secretion, and prediabetes: in vitro and population-based studies. *Front Endocrinol. (Lausanne)* **14**, 1195658 (2023).
57. Anwar, M. M. & Mabrouk, A. A. Hepatic and cardiac implications of increased toxic amyloid-beta serum level in lipopolysaccharide-induced neuroinflammation in rats: new insights into alleviating therapeutic interventions. *Inflammopharmacology* **31**, 1257–1277 (2023).
58. Villeda, S. A. et al. Young blood reverses age-related impairments in cognitive function and synaptic plasticity in mice. *Nat. Med* **20**, 659–663 (2014).
59. Katsimpardi, L. et al. Vascular and neurogenic rejuvenation of the aging mouse brain by young systemic factors. *Science* **344**, 630–634 (2014).
60. Xia, E. et al. Young blood rescues the cognition of alzheimer's model mice by restoring the hippocampal cholinergic circuit. *Neuroscience* **417**, 57–69 (2019).
61. Alfonso, J., Penkert, H., Duman, C., Zuccotti, A. & Monyer, H. Downregulation of Sphingosine 1-Phosphate Receptor 1 Promotes the Switch from Tangential to Radial Migration in the OB. *J. Neurosci.* **35**, 13659–13672 (2015).
62. Bao, X. et al. Sphingosine 1-phosphate promotes the proliferation of olfactory ensheathing cells through YAP signaling and participates in the formation of olfactory nerve layer. *Glia* **68**, 1757–1774 (2020).
63. Waeber, C. & Chiu, M. L. In vitro autoradiographic visualization of guanosine-5'-O-(3-[35S]thio)triphosphate binding stimulated by sphingosine 1-phosphate and lysophosphatidic acid. *J. Neurochem* **73**, 1212–1221 (1999).
64. Borowsky, A. D. et al. Sphingosine-1-phosphate lyase expression in embryonic and adult murine tissues. *J. Lipid Res* **53**, 1920–1931 (2012).
65. Porlan, E. et al. MT5-MMP regulates adult neural stem cell functional quiescence through the cleavage of N-cadherin. *Nat. Cell Biol.* **16**, 629–638 (2014).
66. Kokovay, E. et al. VCAM1 is essential to maintain the structure of the SVZ niche and acts as an environmental sensor to regulate SVZ lineage progression. *Cell Stem Cell* **11**, 220–230 (2012).
67. Khoonsari, P. E. et al. Analysis of the Cerebrospinal Fluid Proteome in Alzheimer's Disease. *PLoS One* **11**, e0150672 (2016).
68. Vojinovic, D. et al. Genome-wide association study of 23,500 individuals identifies 7 loci associated with brain ventricular volume. *Nat. Commun.* **9**, 3945 (2018).
69. Podlesek, D. et al. Olfactory bulb volume in patients with idiopathic normal pressure hydrocephalus. *Neuroradiology* **54**, 1229–1233 (2012).
70. Yamada, S., Ishikawa, M. & Nozaki, K. Exploring mechanisms of ventricular enlargement in idiopathic normal pressure hydrocephalus: a role of cerebrospinal fluid dynamics and motile cilia. *Fluids Barriers CNS* **18**, 20 (2021).
71. Müller-Schmitz, K. et al. Normal Pressure Hydrocephalus Associated with Alzheimer's Disease. *Ann. Neurol.* **88**, 703–711 (2020).
72. Luikku, A. J. et al. Predicting Development of Alzheimer's Disease in Patients with Shunted Idiopathic Normal Pressure Hydrocephalus. *J. Alzheimers Dis.* **71**, 1233–1243 (2019).
73. Khasawneh, A. H., Garling, R. J. & Harris, C. A. Cerebrospinal fluid circulation: What do we know and how do we know it?. *Brain Circ.* **4**, 14–18 (2018).
74. Iliff, J. J. et al. A paravascular pathway facilitates CSF flow through the brain parenchyma and the clearance of interstitial solutes, including amyloid β. *Sci. Transl. Med* **4**, 147ra111 (2012).
75. Tarasoff-Conway, J. M. et al. Clearance systems in the brain-implications for Alzheimer disease. *Nat. Rev. Neurol.* **11**, 457–470 (2015).
76. Da Mesquita, S. et al. Functional aspects of meningeal lymphatics in ageing and Alzheimer's disease. *Nature* **560**, 185–191 (2018).
77. Igarashi, J. & Michel, T. Sphingosine-1-phosphate and modulation of vascular tone. *Cardiovasc Res* **82**, 212–220 (2009).
78. Bravo, G., Cedeño, R. R., Casadevall, M. P. & Ramió-Torrentà, L. Sphingosine-1-Phosphate (S1P) and S1P Signaling Pathway

Modulators, from Current Insights to Future Perspectives. *Cells* **11**, 2058 (2022).
79. Babcock, K. R., Page, J. S., Fallon, J. R. & Webb, A. E. Adult Hippocampal Neurogenesis in Aging and Alzheimer's Disease. *Stem Cell Rep.* **16**, 681–693 (2021).
80. Kim, H. S. et al. Relationship between adult subventricular neurogenesis and Alzheimer's disease: Pathologic roles and therapeutic implications. *Front Aging Neurosci.* **14**, 1002281 (2022).
81. Ziabreva, I. et al. Altered neurogenesis in Alzheimer's disease. *J. Psychosom. Res* **61**, 311–316 (2006).
82. Youn, Y. C. et al. Blood amyloid-β oligomerization associated with neurodegeneration of Alzheimer's disease. *Alzheimers Res Ther.* **11**, 40 (2019).
83. Shim, K. H. et al. Subsequent correlated changes in complement component 3 and amyloid beta oligomers in the blood of patients with Alzheimer's disease. *Alzheimers Dement* **20**, 2731–2741 (2024).
84. Cummings, J. et al. Alzheimer's disease drug development pipeline: 2023. *Alzheimers Dement (N. Y)* **9**, e12385 (2023).
85. Ganat, Y. M. et al. Early postnatal astroglial cells produce multilineage precursors and neural stem cells in vivo. *J. Neurosci.* **26**, 8609–8621 (2006).
86. Christensen, P. M., Bosteen, M. H., Hajny, S., Nielsen, L. B. & Christoffersen, C. Apolipoprotein M mediates sphingosine-1-phosphate efflux from erythrocytes. *Sci. Rep.* **7**, 14983 (2017).
87. Kobayashi, N., Kobayashi, N., Yamaguchi, A. & Nishi, T. Characterization of the ATP-dependent sphingosine 1-phosphate transporter in rat erythrocytes. *J. Biol. Chem.* **284**, 21192–21200 (2009).
88. Nguyen, T. Q. et al. Erythrocytes efficiently utilize exogenous sphingosines for S1P synthesis and export via Mfsd2b. *J. Biol. Chem.* **296**, 100201 (2021).
89. Bicker, F. et al. Neurovascular EGFL7 regulates adult neurogenesis in the subventricular zone and thereby affects olfactory perception. *Nat. Commun.* **8**, 15922 (2017).
90. Vancamp, P. et al. Developmental thyroid disruption permanently affects the neuroglial output in the murine subventricular zone. *Stem Cell Rep.* **17**, 459–474 (2022).
91. Vancamp, P. et al. Gender-specific effects of transthyretin on neural stem cell fate in the subventricular zone of the adult mouse. *Sci. Rep.* **9**, 19689 (2019).
92. Jiang, Z. et al. MT1-MMP deficiency leads to defective ependymal cell maturation, impaired ciliogenesis, and hydrocephalus. *JCI Insight* **5**, e132782 (2020).
93. Palavicini, J. P. et al. Sulfatide Deficiency, an Early Alzheimer's Lipidomic Signature, Causes Brain Ventricular Enlargement in the Absence of Classical Neuropathological Hallmarks. *Int J. Mol. Sci.* **24**, 233 (2022).
94. Zhu, Y. et al. Hemopexin is required for adult neurogenesis in the subventricular zone/olfactory bulb pathway. *Cell Death Dis.* **9**, 268 (2018).
95. Mirzadeh, Z., Doetsch, F., Sawamoto, K., Wichterle, H. & Alvarez-Buylla, A. The subventricular zone en-face: wholemount staining and ependymal flow. *J. Vis. Exp.* **39**, 1938 (2010).
96. Ryan, U. S. & Hart, M. A. Electron microscopy of endothelial cells in culture: II. Scanning electron microscopy and OTOTO impregnation method. *J. tissue Cult. methods* **10**, 35–36 (1986).
97. Seo, J. S., Mantas, I., Svenningsson, P. & Greengard, P. Ependymal cells-CSF flow regulates stress-induced depression. *Mol. Psychiatry* **26**, 7308–7315 (2021).
98. Fedorov, A. et al. 3D Slicer as an image computing platform for the Quantitative Imaging Network. *Magn. Reson Imaging* **30**, 1323–1341 (2012).
99. Yue, N. C. et al. Sulcal, ventricular, and white matter changes at MR imaging in the aging brain: data from the cardiovascular health study. *Radiology* **202**, 33–39 (1997).
100. Velagapudi, S. et al. Apolipoprotein M and Sphingosine-1-Phosphate Receptor 1 Promote the Transendothelial Transport of High-Density Lipoprotein. *Arterioscler Thromb. Vasc. Biol.* **41**, e468–e479 (2021).
101. Christensen, P. M. et al. Impaired endothelial barrier function in apolipoprotein M-deficient mice is dependent on sphingosine-1-phosphate receptor 1. *Faseb j.* **30**, 2351–2359 (2016).
102. Takahashi, H. & Tsuboi, A. Olfactory Avoidance Test (Mouse). *Bio Protoc.* **7**, e2153 (2017).
103. Takahashi, H. et al. A subtype of olfactory bulb interneurons is required for odor detection and discrimination behaviors. *J. Neurosci.* **36**, 8210–8227 (2016).
104. Akers, K. G. et al. Fetal alcohol exposure leads to abnormal olfactory bulb development and impaired odor discrimination in adult mice. *Mol. Brain* **4**, 29 (2011).
105. Aqrabawi, A. J. et al. Top-down modulation of olfactory-guided behaviours by the anterior olfactory nucleus pars medialis and ventral hippocampus. *Nat. Commun.* **7**, 13721 (2016).
106. Belenguer, G., Domingo-Muelas, A., Ferrón, S. R., Morante-Redolat, J. M. & Fariñas, I. Isolation, culture and analysis of adult subependymal neural stem cells. *Differentiation* **91**, 28–41 (2016).
107. Song, H., Stevens, C. F. & Gage, F. H. Astroglia induce neurogenesis from adult neural stem cells. *Nature* **417**, 39–44 (2002).
108. Ferrón, S. R. et al. Postnatal loss of Dlk1 imprinting in stem cells and niche astrocytes regulates neurogenesis. *Nature* **475**, 381–385 (2011).
109. Hirrlinger, J. et al. Split-cre complementation indicates coincident activity of different genes in vivo. *PLoS One* **4**, e4286 (2009).
110. Chin, C. H. et al. cytoHubba: identifying hub objects and sub-networks from complex interactome. *BMC Syst. Biol.* **8**, S11 (2014).
111. Doty, R. L., Marcus, A. & Lee, W. W. Development of the 12-item Cross-Cultural Smell Identification Test (CC-SIT). *Laryngoscope* **106**, 353–356 (1996).
112. Winkler, E. A. et al. GLUT1 reductions exacerbate Alzheimer's disease vasculo-neuronal dysfunction and degeneration. *Nat. Neurosci.* **18**, 521–530 (2015).

Acknowledgements

This research was supported by the Bio&Medical Technology Development Program of the National Research Foundation (NRF) funded by the Korean government (MSIT) (RS-2023-00226494 to H.K.J). This work was also supported by a grant of the Korea Dementia Research Project through the Korea Dementia Research Center (KDRC), funded by the Ministry of Health & Welfare and Ministry of Science and ICT, Republic of Korea (RS-2023-KH137702 to J.S.B)

Author contributions

B.J.C. designed and performed experiments and wrote the paper. J.Y.H., M.H.P., K.H.P., W.H.H., H.J.Y., H.Y.J., K.Y.K., S.A.L., E.Y.L, and J.W.H. performed experiments and analyzed data. I.S.S., S.Y.J., and M.K.C. performed LC-MS/MS experiments and analyzed data. C.C. generated and provided *Apom*$^{-/-}$ and *Apom*^{TG} mice and contributed to the interpretation of the results. H.J.K. and S.H.K. performed normal, PD, and AD patient experiments. S.H.K., E.H.S., H.K.J., and J.S.B. interpreted the data and reviewed the paper. H.K.J. and J.S.B. designed the study and wrote the paper. All authors discussed results and commented on the manuscript.

Competing interests

The authors declare no competing interests.

Additional information

Supplementary information The online version contains supplementary material available at https://doi.org/10.1038/s41467-025-60750-0.

Correspondence and requests for materials should be addressed to Jae-sung Bae or Hee Kyung Jin.

Peer review information *Nature Communications* thanks Timothy Hla, Dushani Ranasinghe, Francis Szele and the other, anonymous, reviewer for their contribution to the peer review of this work. A peer review file is available.